Nano-grooving by Using Multi-tip Diamond Tools

4

Xichun Luo and Zhen Tong

Contents

X. Luo (✉)
Centre for Precision Manufacturing, Department of Design, Manufacture and Engineering Management, University of Strathclyde, Glasgow, UK
e-mail: Xichun.luo@strath.ac.uk

Z. Tong
Centre for Precision Manufacturing, Department of Design, Manufacture and Engineering Management, University of Strathclyde, Glasgow, UK

Centre for Precision Technologies, University of Huddersfield, Huddersfield, UK
e-mail: Z.Tong@hud.ac.uk

Abstract

This chapter introduces nano-grooving approach by using multi-tip diamond tools to generate nanostructures such as nano-gratings/nano-grooves on large substrates. It starts by briefing the work principle and history of this nanofabrication approach. It then introduces the machining mechanism, influences of processing parameters, and tool wear on the machined nanostructures. It concludes with a summary of research challenges, current research achievements, and future research directions to systematically establish this nanofabrication approach.

4.1   Introduction

Fabrication of periodic micro- and nanostructures over a large area has attracted great interest in recent years due to growing applications of such functional structures in optics, automotive, aerospace, biomedical, and power generation devices (Holmberg et al. 2014; Bartolo et al. 2012; Berman and Krim 2013; Kaur and Singh 2014). For example, periodic nano-grating is a typical nanostructure for the excitation of surface plasmon resonance (Atwater and Polman 2010; Liu et al. 2005). It is the basis of many resonance-coupling-based plasmonic devices such as the plasmonic solar cell (Mokkapati et al. 2009; Akimov and Koh 2010) and the surface-enhanced Raman spectroscopy (SERS) for the massively enhancing adsorption of signal onto planar metal surfaces (Clark and Cooper 2011).

Several nanofabrication techniques are currently used to obtain nanostructured surfaces, such as focused ion beam (FIB) machining, laser machining, optical lithography (EUV, UV, and X-ray lithography, etc.), electron beam lithography, nanoimprint lithography (NIL), and scanning probe lithography. Apart from these techniques, ultra-precision diamond turning is another promising approach to obtain nanostructures in a repeatable and cost-effective manner while maintaining high precision. The work principle of this new nano-grooving approach is illustrated in Fig. 1. It can be seen that the nano-gratings/nano-grooves are generated on the workpiece surface by plunging cut using a diamond tool with prefabricated nano-grating structures on its tip. By this method many gratings/grooves can be generated in one single cutting pass.

The crystalline structure of diamond permits the fabrication of cutting tools with very sharp cutting edges which result in nanometer-level surface finish for these nanostructures after a single cutting pass. Varieties of tool geometries, such as single-tipped and dual-tipped tools having rectangular-, triangular-, and other complex-shaped face designs, have been produced to generate functional structured surfaces through ultra-precision diamond turning process (Picard et al. 2003; Ding et al.

Fig. 1 Work principle of
nano-grooving by using
multi-tip diamond tool
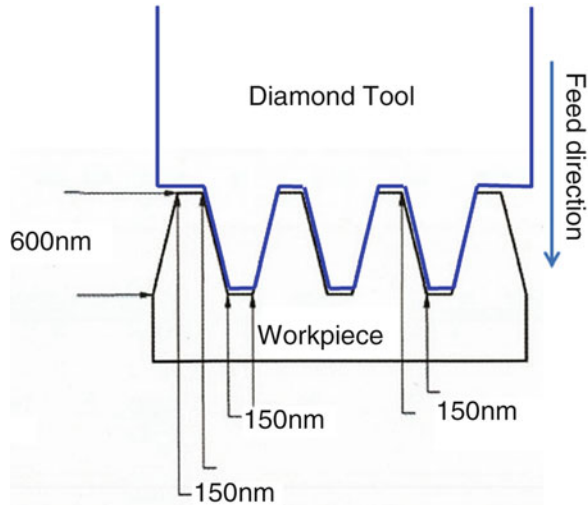
2008; Xu et al. 2010). Moreover, ultra-precision diamond turning technique also
offers an opportunity to cave 3D structures on nonplanar surfaces (Davies et al.
2003). This approach, therefore, fully utilizes the fine process capability of the
physical sputtering actions of the FIB and the high productivity of diamond turning.
This chapter will introduce the history of nano-grooving approach, machining
mechanism, and influences of processing parameters and tool wear on the generated
nanostructures.

4.2   Brief History

Nano-grooving by using a multi-tip diamond tool is inspired by the pioneering work
of Friedrich and Vasile et al. for the fabrication of microstructures (Friedrich and
Vasile 1996; Vasile et al. 1996, 1999; Friedrich et al. 1997). They used FIB milling to
produce nominal 25 μm diameter micro tools used on an ultra-precision machining
center. Because of the Gaussian ion beam intensity profile, the cutting edge near the
ion beam is rounded off and other edges away from the beam become sharper
(Friedrich and Vasile 1996; Vasile et al. 1996).

   Picard et al. (2003) from Sandia National Laboratories (SNL) presented the
method of FIB shaping micro-scale tools (with dimensions in a range of
15–100 μm) analogous to a cutting tool used in lathes. They proposed a procedure
for shaping a two-tip micro cutting tool (as shown in Fig. 2). The cutting tools having
rectangular, triangular, and trapezoid shapes were successfully fabricated by FIB.
Among the tested tool materials, diamond and tungsten carbide materials are easier
to form a sharp cutting edge than high-speed steel. These tools were further applied
for ultra-precision machining of microgrooves, microcoils, and curvilinear structures
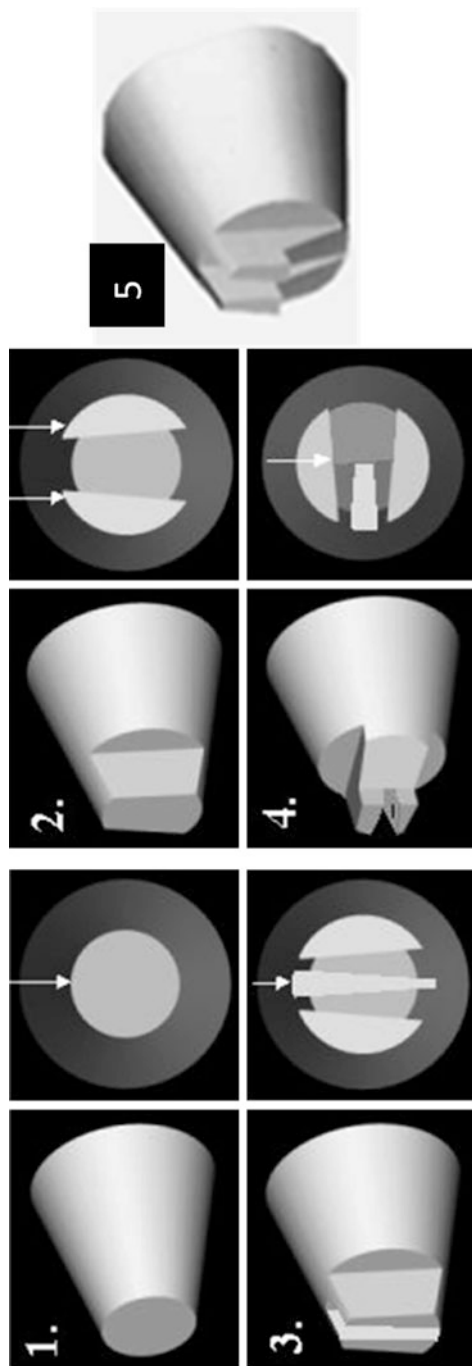(as shown in Fig. 3).

Fig. 2 The procedures for FIB milling a micro-threading tool. For all sputter steps, a tool is fixed, and the arrows indicate the direction of the ion beam (Picard et al. 2003)
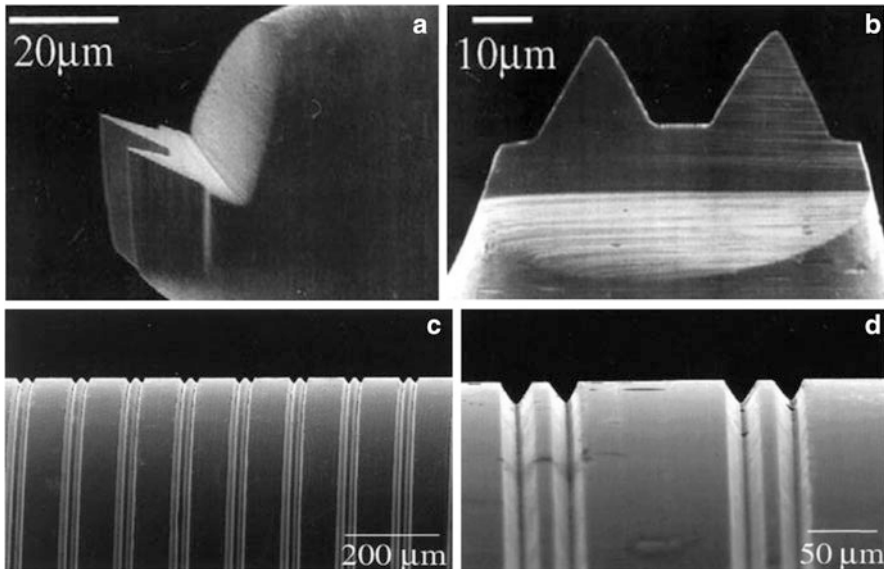
Fig. 3 FIB-shaped two-tip micro tool having triangular cutting faces and the machined micro-grooves. (**a**) and (**b**) show the tool tips; (**c**) and (**d**) show the machined grooves on PEEK workpiece surface by the two-tip tool (Picard et al. 2003)

Ding et al. (2008, 2012) evaluated the dependence of machining removal rate and surface morphology of FIB-sputtered diamond on FIB processing parameters such as the beam current and the ion incident angle. Their results indicate that a single crystal diamond tool fabricated by FIB under lower beam current of 4.6 nA offers a smoother cutting edge and a better tool surface quality as compared to that generated at a current of 20 nA (Ding et al. 2008).

Xu, Zhang, and their co-workers (2010; Zhang et al. 2009) developed semicircular micro tools and diffractive optical elements (DOE)-shaped micro tools to fabricate micro-DOE (MDOE) which are widely used in solar condense lenses, infrared sensors, laser beam shaping, and high-performance optical imaging systems. The measured radius of cutting edges of the micro tool was approximately 25 nm (Xu et al. 2010). The DOE-shaped micro tool and the machined MDOE are shown in Fig. 4 in which nanoscale surface finish was obtained.

Most recently, nano-gratings with the pitch as small as hundreds of nanometres has been generated by using nanoscale multi-tip diamond tools (with tool tip width of 150 nm) by Sun et al. (2012; Sun and Luo 2014). They proposed a divergence compensation method to facilitate FIB machining of nanoscale 3D structures. Through adjusting key fabrication parameters such as dwell time distribution, scanning passes, scanning pitch, and scanning strategy, they successfully fabricated a nanoscale diamond cutting tool with nanoscale periodical chisel structures on the tool tip as shown in Fig. 5. Initial results of using the nanoscale multi-tip diamond tool in the scratching of nano-grating arrays on an electroless nickel substrate show a
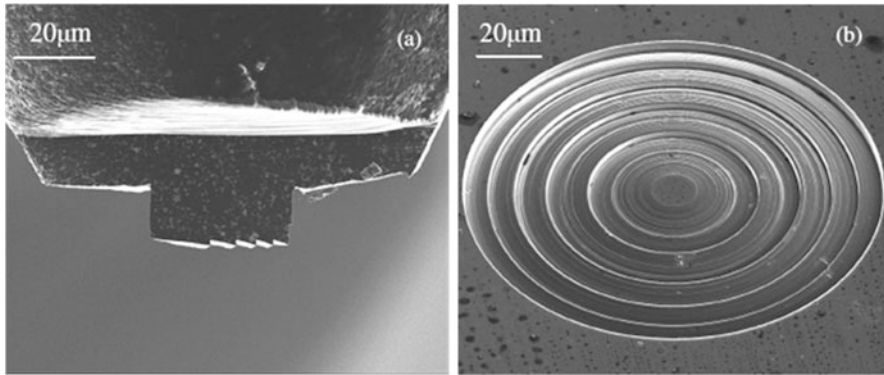
Fig. 4 SEM images of MDOE fabricated by a DOE-shaped micro tool. (**a**) DOE-shaped micro tool by FIB, (**b**) MDOE machined by the DOE-shaped micro tool (Xu et al. 2010)
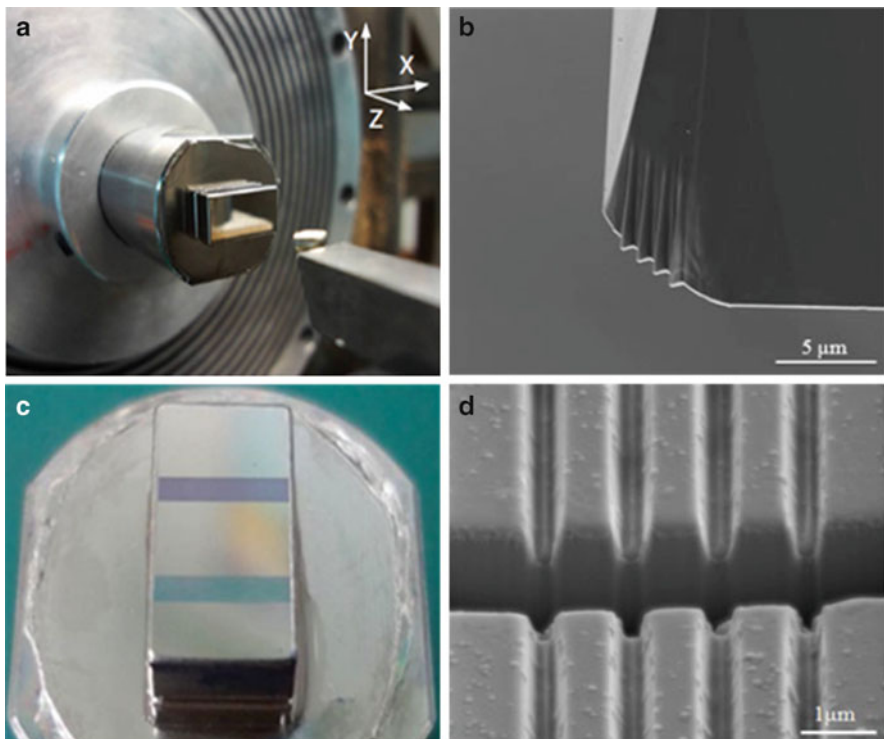
Fig. 5 Diamond machining of nano-grating arrays using a nanoscale multi-tip diamond tool. (**a**) Experimental setup of the ultra-precision diamond turning test; (**b**) SEM image of the nanoscale multi-tip diamond tool; (**c**) nano-grating arrays fabricated in two regions on the Nickel sample surface; and (**d**) the cross-sectional view of the machined nano-grating arrays (Sun et al. 2012)

high machining efficiency. The material removal rate was proved to be 30,000 times higher than purely FIB machining with ion current of 1 nA when machining these nanostructures (Sun et al. 2012). Since then, nano-grooving technique has been extensively studied by researchers to explore its manufacturing capability (Tong et al. 2014a, b, 2015a; Luo et al. 2014). The following session will introduce these studies from the aspects of machining mechanism, influence of processing parameters, and tool wear on the generated nanostructures.

4.3   Machining Mechanism

While using a nanoscale multi-tip cutting tool, the nanostructures are synchronously generated through a single cutting pass. The material removal process in a nanoscale multi-tip tool cutting will be different from that of using a single-tip cutting tool. In-depth understanding of the nanostructure formation process during multi-tip tool cutting is a necessity to further improve the nanomanufacturing capacity of this technique. To overcome the limitation in real-time experimental observation molecular dynamics (MD), simulations are often used by researchers to reveal the machining mechanism and obtain valuable feedback and guidance for further development of this new technique. In this session, the nanostructure generation processes, when using a single-tip and a multi-tip diamond tool, are modelled by MD simulation method. In order to benchmark the advantages and disadvantages of diamond turning using nanoscale multi-tip diamond tools, a comparison between using single-tip and multi-tip nanoscale tools in nanometric cutting is made from the viewpoint of nanostructure generation, cutting forces, and cutting temperature.

4.3.1   MD Nanometric Cutting Model

Geometric model for MD simulation: The geometry of the cutting tools is shown in Figs. 6a and 6b. Both the single-tip and the multi-tip diamond tool models are created based on the perfect diamond crystal structure. The tool-tip width is $W_a = 15a_1$ ($a_1 = 3.567$ Å) with the tool rake angle α being 0° and the tool clearance angle β being 12°. To save the computational time, a nanoscale double-tip diamond tool with a pitch of $L = 10a_1$ is employed in current research to represent the nanoscale multi-tip diamond tool. Since the radius of the cutting edge of the diamond tool is usually larger than the minimum depth of cut in nanometric cutting, in present large-scale MD simulations, all the tool models are built with a round cutting edge with the edge radius of $r = 5a_1$ instead of sharp cutting edges.

The workpiece has a dimension of $50a_2 \times 80a_2 \times 40a_2$ ($a_2 = 3.615$ Å is the lattice constant of copper) and consists of a boundary layer and a thermostat layer with thicknesses of $2a_2$ and $3a_2$, respectively (as shown in Fig. 6c and d). The three orientations of the workpiece are [1 0 0], [0 1 0], and [0 0 1] in the X, Y, and Z directions. Free boundary conditions are applied in all directions. Both the nanosized workpiece and the diamond cutting tool were modelled as deformable bodies.
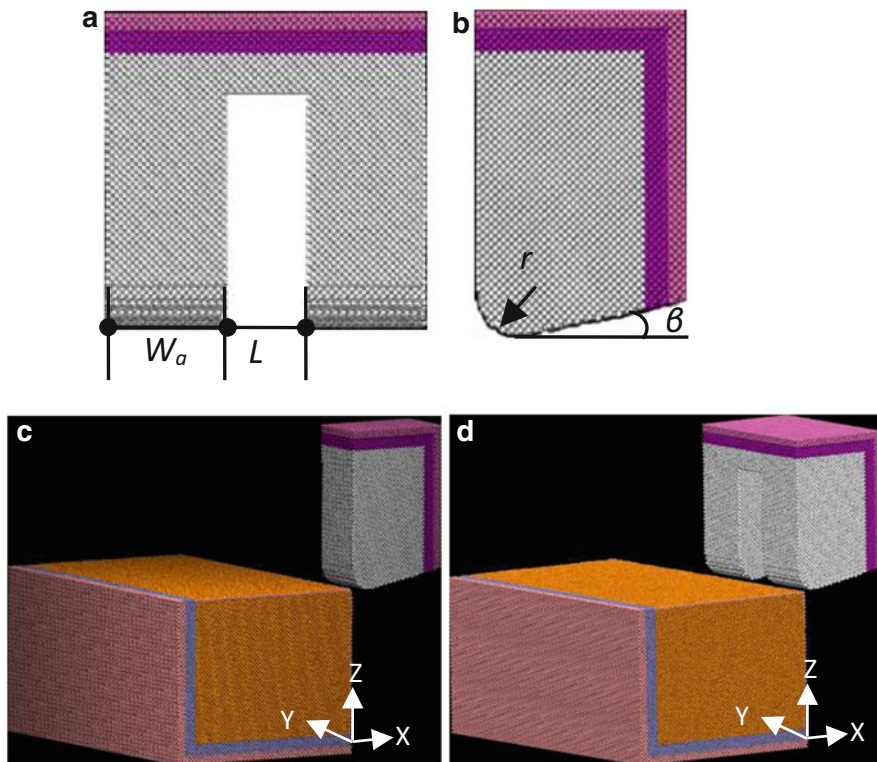
Fig. 6 Models of MD nanometric cutting simulation. (**a**) Front view of the multi-tip tool model; (**b**) right-hand end elevation of the tool tip model; (**c**) single-tip tool cutting model; and (**d**) multi-tip tool cutting model (Tong et al. 2014a)

During nanometric cutting, the bottom and outer sides of the substrate (atoms in pink color) are fixed as it has been suggested to be an appropriate configuration to simulate the nanometric cutting process (Lin and Huang 2008; Zhu et al. 2010).

Potential functions: In nanometric cutting, hybrid potential functions can be used to describe the interactions between the tool and the workpiece as well as the quantum interactions between electron shells and represent the physical properties of each atom type being simulated, such as elastic constants and lattice parameters. Balamane et al. (1992) and Smith et al. (2004) have presented a comprehensive review of the potential energy functions that have been used in recent decades.

In nanometric cutting of copper, there are three different atomic interactions in the MD simulation: (1) the interaction between copper atoms (Cu–Cu) of the workpiece, (2) the interaction between diamond atoms (C–C) of the tool, and (3) the interaction between workpiece and tool (Cu–C). For the Cu–Cu interaction, the embedded atom method (EAM) potential proposed by Foiles et al. (Daw et al. 1993) is used since it has been widely used in description of metallic materials (Ye et al. 2003; Pei et al. 2009; Pelaz et al. 2004). As it is shown in Eq. 1, the total energy E_{eam} of the atomistic

system comprises summation over the atomistic aggregate of the individual embedding energy F^i of atom i and pair potential ϕ_{ij} between atom i and its neighboring atom j, which can be expressed as:

$$E_{eam} = \sum_i F^i \left(\sum_{j \neq i}^{n} \rho^i \left(r^{ij} \right) \right) + \frac{1}{2} \sum_{ij, i \neq j} \phi_{ij} \left(r^{ij} \right) \tag{1}$$

where the E_{eam} is the total energy of the atomistic system which comprises summation over the atomistic aggregate of the individual embedding energy F^i of atom i and the pair potential ϕ_{ij} between atom i and its neighboring atom j. The lower case Latin superscripts i and j refer to the different atoms, r^{ij} is the distance between the atoms i and j, and $\rho^i(r^{ij})$ is the electron density of the atom i contributed by atom j.

For C–C atoms, we adopt the Tersoff potential (Tersoff 1989) computed as follows:

$$V_{ij} = f_C \left(r_{ij} \right) \left[f_R \left(r_{ij} \right) + b_{ij} f_A \left(r_{ij} \right) \right] \tag{2}$$

where V_{ij} is the bond energy, i and j label the atoms of the system, r_{ij} is the length of the ij bond, b_{ij} is the bond order term, f_R is a two-body term, f_A includes three-body interactions, and f_C represents a smooth cutoff function to limit the range of the potential.

The Morse potential function (Ikawa et al. 1991a) was used to describe the interaction between Cu and C, and the total energy E_{tot} is expressed as:

$$E_{tot} = \sum_{ij} D_0 \left[e^{-2\alpha \left(r - r_p \right)} - 2e^{-\alpha \left(r - r_p \right)} \right] \tag{3}$$

where r is the instantaneous distance between atoms i and j. The cohesion energy D_0, the elastic modulus α, and the equilibrium bond distance r_p are 0.087 eV, 5.14 Å^{-1}, and 2.05 Å, respectively (Ikawa et al. 1991a).

## 4.3.2 MD Simulation Setup

All of the cutting tools are applied along the $[-1\ 0\ 0]$ direction on the $(0\ 0\ 1)$ surface of the copper at a constant cutting speed of 200 m/s. Of course, the simulation may have its own limitations including the need to run at very high cutting speeds, but this may not be a serious limitation as long as we are interested in the general nature of the process without consideration of the speed effects (Komanduri et al. 2001). The main computational parameters used in the MD simulations are summarized in Table 1 for reference.

The equations of atom motion were integrated using velocity Verlet algorithm with a time step of 1 fs. Moreover, 85,000 time steps were carried out as the relaxation process to adjust the system to 293 K before cutting. During cutting and the thermal annealing processes, the systems were controlled by NVE ensemble, and the thermostat atoms were kept at a constant temperature of 293 K through a velocity

Table 1 MD simulation parameters for nanometric cutting of copper (Tong et al. 2014a)

	Single-tip with multi-pass	Multi-tip with single pass
Workpiece material	Copper	Copper
Workpiece dimension	$50a_2 \times 80a_2 \times 40a_2$ ($a_2 = 3.615$ Å)	$50a_2 \times 80a_2 \times 40a_2$ ($a_2 = 3.615$ Å)
Number of atoms	760, 355	894, 870
Tool tip width	$15a_1$ ($a_1 = 3.567$ Å)	$15a_1$ ($a_1 = 3.567$ Å)
Tool rake angle	0°	0°
Tool clearance angle	12°	12°
Time step	1 fs	1 fs
Initial temperature	293 K	293 K
Depth of cut	1 nm	1 nm
Cutting speed	200 m/s	200 m/s
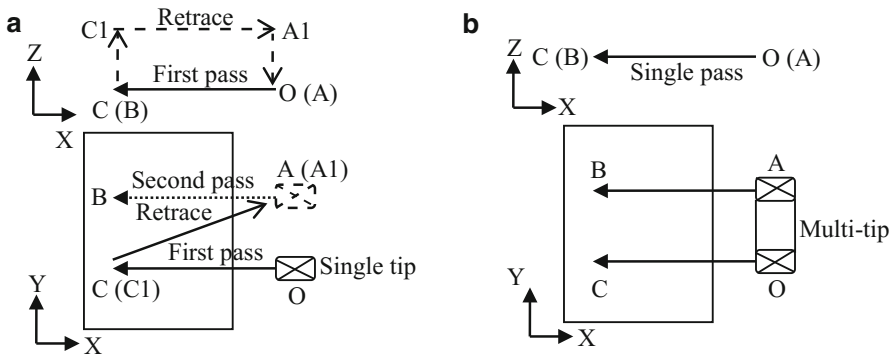
Fig. 7 (**a**) Single-tip cutting with two passes; (**b**) multi-tip cutting with single pass (Tong et al. 2014a)

scaling method to perform the heat dissipation (Yan et al. 2007). The velocity scaling method controls the temperature by rescaling the thermal atoms velocities to 293 K if the temperature departs more than 5 K from the specified temperature at a certain time step. Thus, this algorithm allows the heat transferring from shear region to the bulk of the workpiece which conforms to experimental observation.

Figure 7 shows the simulation procedure of nanometric cutting and traces of the tool. For a single-tip tool, it scratched the surface in X-Y plane along the OC direction for the first cutting pass (as shown in Fig. 7a). Then the tool followed trace (C–C1) in the Y-Z plane. The tool moved along line C1A1 and moved down to point A. At last, the tool scratched the second groove along the line AB with same depth of cut (as the dotted line shows). For multi-tip tool, only single pass was taken with the same cutting distance as shown in Fig. 7b. All the simulations were performed by a high-performance computing cluster (HPC) using 24 cores.

4.3.3   The Post-processing Methods

Calculation of the stresses and cutting forces: In LAMMPS, the stress for each atom is attributed to its interaction with all other atoms in the simulation, and the stress tensor for an atom i can be calculated from Eq. 4.

$$
\begin{aligned}
S_{ab} = & \left[\begin{array}{l}
mv_a v_b + \dfrac{1}{2} \sum_{n=1}^{N_p} \left(r_{1_a} F_{1b} + r_{2_a} F_{2b} \right) + \dfrac{1}{2} \sum_{n=1}^{N_b} \left(r_{1_a} F_{1b} + r_{2_a} F_{2b} \right) \\[3mm]
-\quad +\dfrac{1}{3} \sum_{n=1}^{N_a} \left(r_{1_a} F_{1b} + r_{2_a} F_{2b} + r_{3_a} F_{3b} \right) + \dfrac{1}{4} \sum_{n=1}^{N_d} \left(r_{1_a} F_{1b} + r_{2_a} F_{2b} + r_{3_a} F_{3b} + r_{4_a} F_{4b} \right) \\[3mm]
+\dfrac{1}{4} \sum_{n=1}^{N_i} \left(r_{1_a} F_{1b} + r_{2_a} F_{2b} + r_{3_a} F_{3b} + r_{4_a} F_{4b} \right) + \mathrm{Kspace}\left(r_{ia}, F_{ib} \right)
\end{array} \right]
\end{aligned}
$$

$$(4)$$

where a and b denote x, y, z to generate six components of the symmetric stress tensor. The first term of the equation is a contribution due to the kinetic energy of atom i. The second term is a pair-wise energy contribution where n loops over the N_p neighbors of atom i and r_1 and r_2 are the positions of the two atoms in the pair-wise interaction. F_{1b} and F_{2b} are the forces on the two atoms resulting from the pair-wise interactions. The third term is a bond contribution over the N_b bonds of atom i. There are similar terms for N_a angle, N_d dihedral, and N_i improper interactions. Kspace term represents long-range Coulombic interactions.

The tensor for each atom has six components and is stored as a six-element vector in the following order: σ_{xx}, σ_{yy}, σ_{zz}, τ_{xy}, τ_{xz}, τ_{yz}. However, it is noted that the per-atom stress is really a stress-volume formulation. In order to generate continuous matter, it would need to be divided by a per-atom volume to have units of stress. The hydrostatic stress (σ_{hydro}) and von Mises stress (σ_{von}) can be further computed using the following equations:

$$
\sigma_{hydro} = \frac{\sigma_{xx} + \sigma_{yy} + \sigma_{zz}}{3} \tag{5}
$$

$$
\sigma_{von} = \sqrt{ \frac{ \left(\sigma_{xx} - \sigma_{yy} \right)^2 + \left(\sigma_{xx} - \sigma_{zz} \right)^2 + \left(\sigma_{yy} - \sigma_{zz} \right)^2 + 6 \left(\tau_{xy}^2 + \tau_{yz}^2 + \tau_{xz}^2 \right) }{2} } \tag{6}
$$

For cutting forces, action and reaction are opposite and equal. Since it is quite difficult to accurately measure the volume of the workpiece in cutting zone, the cutting forces were obtained by summing the forces of tool atoms. In LAMMPS, this can be done using "stress/atom" command followed by a "reduce sum" command. A schematic diagram of the forces directions is shown in Fig. 8b.

Calculation of the cutting temperature: Cutting heat has been regarded as one of the key factors to influence the quality of the generated nanostructures as well as the tool life in nanometric cutting process. According to the law of equipartition of
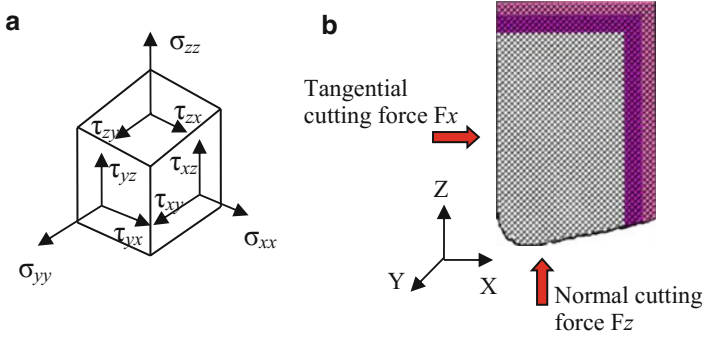
Fig. 8 Schematic diagrams of the stresses and cutting forces. (**a**) Stress directions and (**b**) the direction of cutting forces (Tong et al. 2014a)

energy, the representative temperature of a group of atoms can be calculated from the total atomic kinetic energies of the group. As the nature of the temperature is statistical, the instantaneous kinetic energy of each atom during nanometric cutting differs significantly from the temperature of the bulk. Therefore, the measurement of cutting temperature is not straight forward.

In order to more accurately characterize the variation of temperature during the cutting process, we employed the concept of atomistic equivalent temperature T_i (Tong et al. 2014b) to analyze the cutting temperature. A cutoff distance $r_0 = 4a_0$ was used to select atoms as it can reflect the thermal feature of the short-range structure of copper lattice during nanometric cutting processes. It is noted that only the thermal velocities of atoms are used to compute the temperature. The kinetic energy contributed by the advection movement of the tool should be subtracted beforehand.

CSP: Dislocations play a crucial role in governing the plastic response of ductile materials. The thermal vibration of atoms at finite temperatures makes it difficult to observe dislocations in a thermal-sensitive environment. The widely used methods for tracing such dislocations and other lattice defects are coordinate number analysis, slip vector, and centro-symmetry parameter (CSP). It has been reported that centro-symmetry parameter (CSP) is less sensitive to the temperature increase compared with other methods such as atomic coordinate number and the slip vector (Zong et al. 2010). The CSP method proposed by Kelchner et al. (1998) quantifies local deviations from centro-symmetry in a given centro-symmetric structure such as FCC and BCC (body-centered cubic). The centro-symmetry parameter P_i is defined as follows:

$$P_i = \sum_{i=1}^{6} \left| \vec{R}_i + \vec{R}_{i+6} \right|^2 \tag{7}$$

where $\vec{R}_i$ and $\vec{R}_{i+6}$ are the position vectors corresponding to the six pairs of opposite nearest atoms. The parameter P_i increases from 0 for perfect FCC lattice to positive

Table 2 The default value of atomic structural defects in CSP (Tong et al. 2014a)

CSP value P	Lattice structure	Represent atom color
P < 3	Ideal FCC structure	Yellow
3 < P < 5	Partial dislocation	Cyan
5 < P < 8	Stacking fault	Blue
8 < P < 21.5	Surface atoms	Orange
P > 21.5	Surface atomic step atoms	Pink

values for defects and for atoms close to free surfaces. In the case of the single crystal copper, the default value of P_i corresponding to those atomic defect structures and its representing color are indicated in Table 2.

4.3.4   Nanostructure Generation Process

We first simulated the generation process of nanostructures on the copper surface using the single-tip tool with two cutting passes. The nanostructure in this chapter means a nano-groove machined on the copper surface. It should be noted that the distance between two cutting passes is specified as $10a_1$ ($a_1 = 3.567$ Å) according to the pitch of the multi-tip tool. Figure 9 shows the snapshots of nanometric cutting process as well as the atomistic dislocation evolutions in the workpiece when using the single-tip tool under a depth of cut of 1.0 nm. Every workpiece atom was colored by its CSP value. It should be pointed out that the isolated atoms with a green color inside the workpiece are not lattice defects. Those atoms with CSP above three are caused by thermal vibration at a finite temperature. Moreover, the defect-free atoms were removed from the visualizations.

At initial cutting stage, with the penetration of the tool, the lattice of workpiece deformed as buckled, and the outer kinetic energy of tool transmitted onto the workpiece and converted into potential energy stored in the deformed lattice. When the energy or shear stress of copper atoms exceeds a specific level, the atoms tend to rearrange into lower-energy lattice to relax lattice strain through dislocation nucleation (as shown in Fig. 9a). As the tool advances, more dislocations initiate and propagate in preferred (1 1 1) crystal slip planes systems. The pile-ups of atoms in front of the tool rake face lead to the formation of cutting chip (as shown in Fig. 9b). At the same time, dislocations that penetrated the workpiece migrate out toward the machined surface and create atomic sized steps (atoms in pink color) on the machined surface, which represents the best surface roughness possible.

The second cutting pass was taken along line AB with the same processing parameters (as shown in Fig. 7a). After two consecutive cutting passes, two nano-grooves were machined by the single-tip tool (as shown in Fig. 9c). However, it is found that at the end of the second pass, there were some disordered atoms moved into the first nano-groove. This resulted in the reshaping of the right side of the first machined groove due to the lack of support on that side. This phenomenon is recognized as the feed rate effect in the nanometric cutting. When the distance
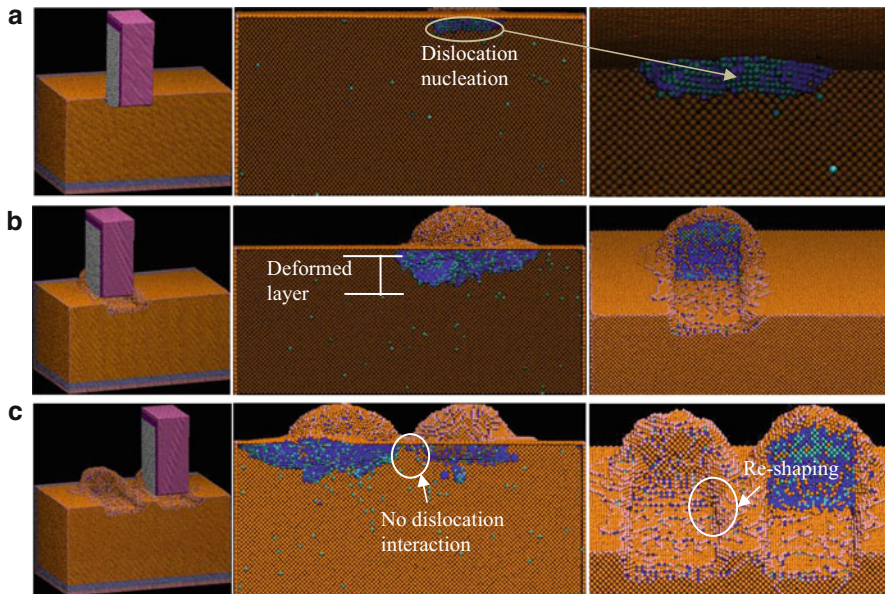
Fig. 9 Snapshots of cutting process and dislocation evolution of workpiece using a single-tip tool with multi-tip passes. (**a**) Dislocation nucleation; (**b**) first cutting pass; and (**c**) the second cutting pass (Tong et al. 2014a)

between two passes is less than a critical value, there is a strong possibility that the material plastic side flow (in terms of dislocation movements) created in the second pass will extend to the machined surface of the first cutting and thus reshape the first nano-groove. It is noted that this critical value is not fixed as the dislocation nucleation and movements are affected by the tool geometry, depth of cut, cutting speed, and local cutting temperature (Zhu et al. 2010).

A similar phenomenon has been reported by Yan et al. (Pei et al. 2009) in their MD study of the AFM scratching of copper. The tool model was built with a round-edged regular three-sided pyramid with a hemisphere at the end (radius of the tool cutting edge of 1 nm). Their investigation showed that the cross-sectional shape of the first scratch was very close to that of the second one when the feed reached 3.62 nm (Pei et al. 2009). Fang et al. (2002) qualitatively compared the feed effect behavior predicted by the MD simulations with the AFM experiments (a diamond AFM tip with radius of 10 nm). Our results agree with their conclusions and further confirm that the feed rate effect also occurs in the rectangular shape tool-tip cutting.

For multi-tip tool cutting, it can be seen from Figs. 10a and 10b that the initial cutting stage was almost the same as that of single-tip tool cutting. The dislocations initiated under the tool-workpiece contact surface due to the compressive stress induced by the initial impact of the tool tips and then propagated along the (1 1 1) crystal slip planes. The atoms accumulated and piled up in front of the multi-tip tool, resulting in the formation of two independent initial chips. The increasing of the chip
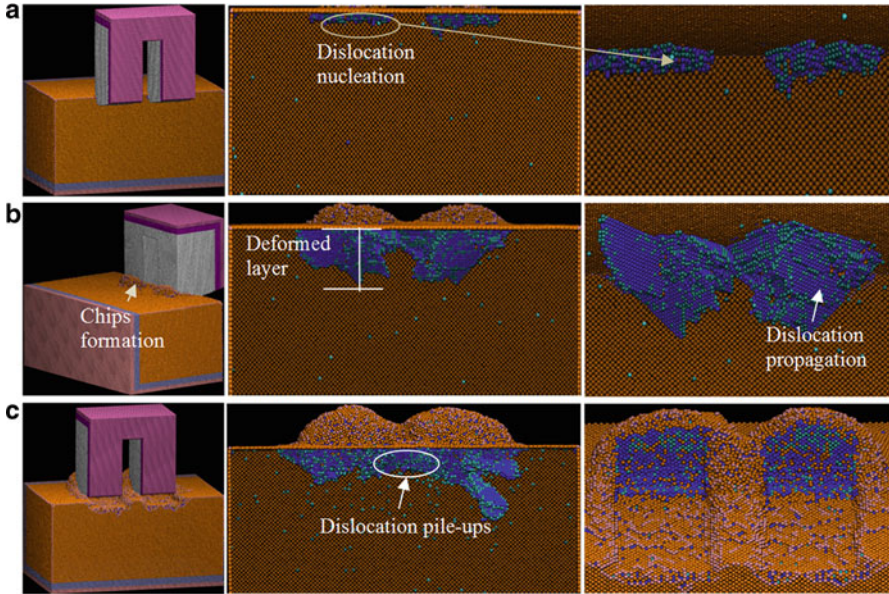
Fig. 10 Snapshots of cutting process and dislocation evolution in workpiece when using the multi-tip tool at cutting distances of (**a**) 2.55 nm, (**b**) 3.95 nm, and (**c**) 15.45 nm (Tong et al. 2014a)

volume indicated that the material deformation states for all cutting conditions were dominated by cutting and accompanied by plough.

However, unlike the single-tip tool cutting, where the nano-grooves were formed through two cutting passes separately, interactions between the dislocations around tool tips were observed when using the multi-tip tool (as shown by Figs. 10b and 10c). Because two nano-grooves were synchronously generated through a single cutting pass, the effect of feed rate observed in single-tip tool cutting can be completely eliminated when using the multi-tip tool. Compared with the nano-groove machined by the single-tip tool cutting, the nano-grooves generated by the multi-tip tool are closer to ideal center line symmetry (Fig. 10c).

4.3.5   Cutting Force

The variations of cutting forces during the steady cutting process were summarized in Fig. 11. The comparison was made between the first and the second cutting pass of the single-tip tool cutting and the multi-tip tool cutting. The results show that the tangential cutting force F_x and normal cutting force F_z in all simulations are fluctuating around an approximately constant value at the steady cutting stage. The dynamic equilibrium of the tool-workpiece contact area and the activities of dislocations accompanying the material removal process are responsible for the fluctuations. Both the normal and tangential cutting forces of the multi-tip tool cutting were
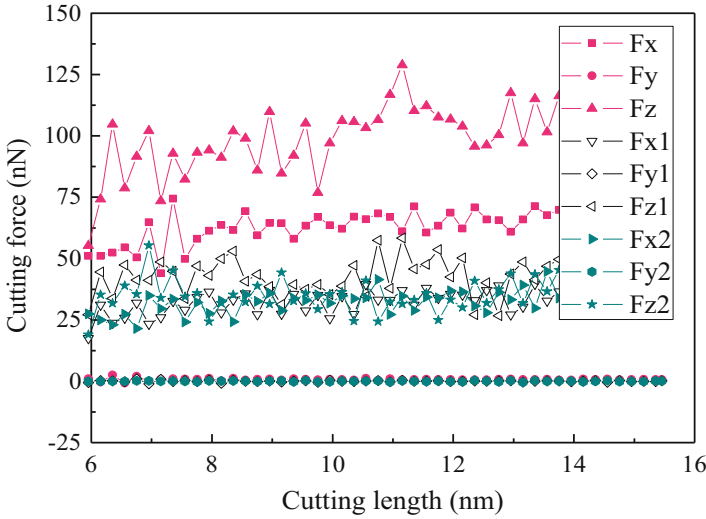
Fig. 11 The force-displacement curves under a depth of cut of 1.0 nm. F_x, F_y, and F_z represent the cutting forces of using the multi-tip tool; F_{x1}, F_{y1}, and F_{z1} and F_{x2}, F_{y2}, and F_{z2} represent the forces for the first and second passes when using the single-tip tool, respectively (Tong et al. 2014a)

larger than those of the single-tip tool cutting (for the first and the second cutting pass). However, the cutting forces in the Y direction were found to have an average value near zero because of the balanced forces contributing from each side.

In order to further quantify the difference of cutting forces between using the single-tip and the multi-tip tool, the average tangential cutting forces and normal cutting forces at the steady cutting state were calculated (as shown in Fig. 12). It was found that the tangential cutting forces of the first and the second cutting passes when using the single-tip tool were nearly the same, but the normal cutting force of the second pass was smaller than that of the first pass. The drop of the normal cutting force resulted from the feed rate effect which appeared at the end of the second cutting pass (as shown in Fig. 9c). The material side flows in terms of the dislocation extension released the extra stress during the second pass and thus lead to a drop of the normal cutting force. For multi-tip tool cutting, while the tangential cutting force per tip has a value of 33.3 nN which is slightly smaller than that of using a single-tip tool, the normal cutting force per tip of 54.1 nN is much larger than those observed when using the single-tip tool (46.9 nN for the first pass, 38.5 nN for the second pass). The significant dislocation pile-ups beneath the tool tips resulted in a local strengthening of the material in the normal direction during the multi-tip cutting process.

Moreover, the ratio of tangential cutting force to normal cutting force ($\mu = F_x/F_z$) is used to assess the alteration of local physical property during the nanometric cutting process. From the average forces at the steady stage, we obtain $\mu \approx 0.61$ for multi-tip cutting and a larger average value of 0.82 for the single-tip tool cutting. Lin et al. have measured the cutting forces in their scratching copper test and found that

Fig. 12 The average cutting forces for the single-tip tool and multi-tip tool cutting (Tong et al. 2014a)
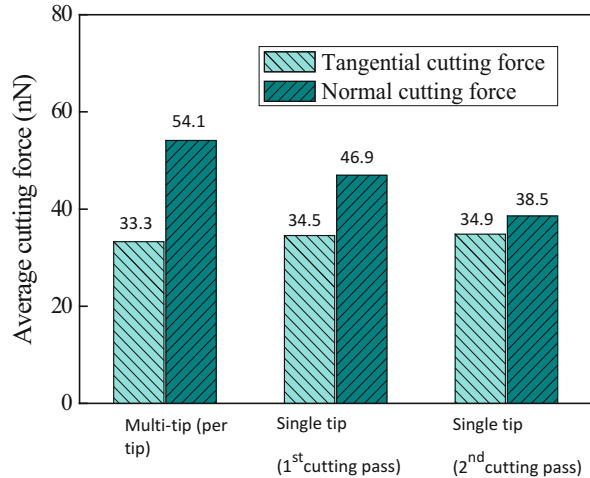
the actual tangential cutting force F_x is 2,780.2 nN and the normal cutting force F_z is 5,686.2 nN (Lin and Huang 2008). The ratio of tangential cutting force to normal cutting force from their experimental data is 0.49. It is noted that our calculated ratio of F_x/F_z is larger than the experimental result because the value also depends on the tool rake angle and surface smoothness and the crystal structure of materials used. Komanduri et al. (2000) have investigated the atomic-scale friction at extremely fine scratch depths (from 0.8 nm to almost zero) and pointed out that for tool built with zero rake angle, the force ratio of F_x/F_z can be as large as 1.170.

Recently, Luan and Robbins have argued that the atomic-scale surface roughness produced by discrete atoms had significant effect on the coefficient of friction, and the contact areas and stresses may be changed with the local alteration of friction and lateral contact stiffness in an order of magnitude (Luan and Robbins 2005). Thus, the difference of the ratio of F_x/F_z observed in the nanometric cuttings between using the single-tip tool and the multi-tip tool may also be attributed to the different local tool-workpiece contact status.

4.3.6   Temperature Distribution

Figure 13 shows the cross-sectional view of the atomistic equivalent temperature distribution for the single-tip tool and the multi-tip tool cuttings. Atoms are colored according to their atomistic equivalent temperature. For better visualization, the white dotted lines are used as the boundaries between the low- and high-temperature zones (>550 K). It was found that in all simulations, the temperature in shear zone was around 650 K. The range of high-temperature region (>550 K) when using the multi-tip tool was apparently larger than that of using the single-tip tool. The highest-temperature regions were found at the tool-chip interface slightly toward the workpiece side.
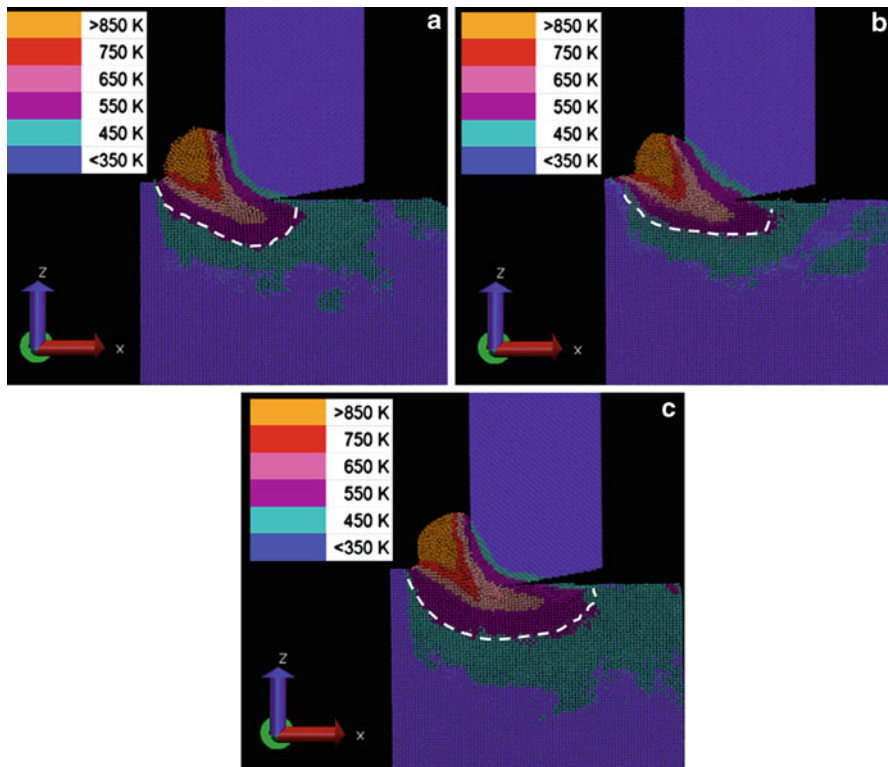
Fig. 13 The cross-sectional views of the temperature distribution at a depth of cut of 17 nm. (**a**) Single-tip cutting (first pass), (**b**) single-tip cutting (second pass), and (**c**) multi-tip cutting with single pass (Tong et al. 2014a)

Unlike traditional metal cutting, in this study the diamond tool material is significantly harder than the workpiece material, i.e., copper. It is a common knowledge that when the cutting tool material is significantly harder than the substrate, the plastic deformation of the softer work material will be the main heat source (Norouzifard and Hamedi 2014). In our MD model, the energy transfer between copper and diamond is described by the selected potential functions. At the interface of the diamond tool and copper substrate, there is an atomic layer (with a thickness of several atoms) which transmits the energy between C and Cu atoms. Copper and the diamond materials both have high thermal conductivity. However, the thermal conductivity of the natural diamond is about 22 W/(cm·K) which is five times more than that for copper. As a result, a large temperature gradient toward the cutting tool was observed in Fig. 13. Moreover, the large diamond cutting tool model built in the present study also helped to release the cutting heat at the tool cutting edge. Therefore, the diamond cutting tool would have lower temperature than the copper substrate, and the highest temperature regions were found at the tool-chip interface slightly toward the workpiece.
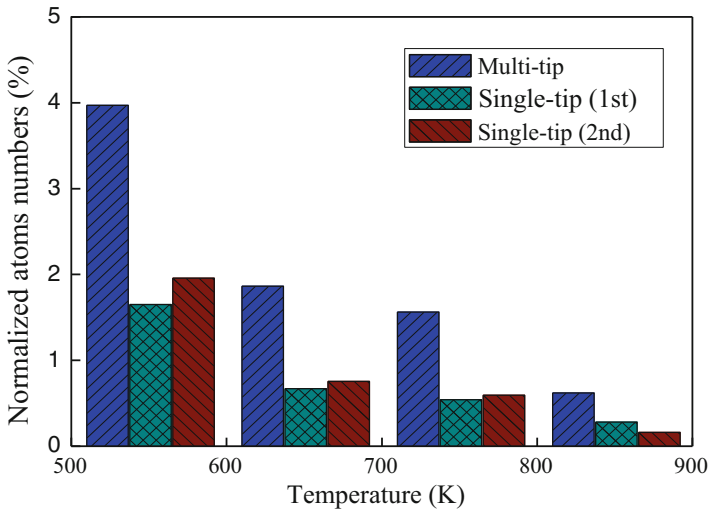
Fig. 14 The normalized atom numbers in different temperature ranges (Tong et al. 2014b)

In order to further quantify the difference in cutting heat when using different kinds of tools, detailed analysis has been done by comparing the number of atoms in different temperature ranges. For a better comparison, only the workpiece atoms within the cutting zone (z coordinate larger than $20a_2$) were taken into account, and the numbers of atoms in different temperature ranges were normalized by the total number of atoms selected (as shown in Fig. 14). It was found that the proportion of atoms with atomistic equivalent temperature larger than 500 K in the multi-tip tool cutting was 8.01% which was apparently larger than that of the single-tip tool cutting (being 3.3%). This result quantitatively demonstrated that the cutting heat generated while using the multi-tip tool was much higher than that of the single-tip tool cutting.

In addition, the higher cutting temperature observed in the multi-tip cutting also explained the feature of cutting forces discussed in the above section. Although the normal cutting force per tip of the multi-tip cutting was larger than that of using the single-tip tool, the tangential cutting force per tip is slightly lower than that of using the single-tip tool. This is mainly due to the fact that the much higher local temperature generated during the multi-tip cutting process would result in local weakening of the Cu–Cu bond force and thus lead to a lower tangential cutting force per tip.

4.3.7   Thermal Annealing at Machined Surface

It has been widely accepted that recrystallization happens during local annealing process, not only in ductile metallic materials but also in brittle materials such as silicon and diamond. In macro machining practice, after the tool has left the machined region, there is a macroscopic time (~ms) for the machined surface to relax (Ye et al. 2003). And by that time, the subsurface atomic defects might be able to get annealed

partly. In a nanometric cutting, the thermal effects happen in such a short timescale that to accurately detect and measure the temperature distribution, it requires a thermal measurement system with extremely short response time and high resolution. However, the spectral wavelength of sensors used in most current commercial infrared thermography are ranging from 0.8 to 14 μm with the response time ranging from 2 to 120 ms. It is therefore very difficult to detect and monitor the nanometric cutting heat accurately by those temperature measurement systems. MD simulation provides an alternative way to solve this problem by allowing the atomistic insight into the material thermal behavior during nanometric cutting processes.

In present work, in order to investigate the thermal effects when different kinds of tools were used, time relaxations of the machined work material were further performed for both the single-tip and multi-tip tool cuttings. It was found through trial simulations that a period of 50 ps relaxation process was enough for the present system to cool down to 293 K. The CSP and the RDF were used to identify the changes in the lattice structure during the relaxation process.

Figure 15 shows the cross-sectional views of the defect zones at 0 and 50 ps. It can be seen that before the relaxation, there are large numbers of dislocations and atomic defects beneath the tool tip (Fig. 15a and c). The thickness of the atomic defect layer formed in the multi-tip tool cutting is about ~6 nm which is nearly twice the thickness created by the single-tip tool cutting (being ~3.5 nm). However, as shown in Fig. 15b, most of atomic defects and dislocations in the machined area were annealed after 50 ps for the single-tip tool cutting. For multi-tip tool cutting, the atomic defects and dislocations were also remarkably annealed after the relaxation process (as shown in Fig. 15d), leaving behind an almost dislocation-free machined workpiece.

In order to further identify the lattice integrity of the machined structure, the RDFs of the machined nano-grooves were calculated. Compared with the single-tip cutting, before relaxation a slightly smaller RDF peak value was found for the nano-grooves machined by the multi-tip tool (Fig. 16a), which indicates that the atoms are in a higher short-range disorder in the multi-tip tool cutting. However, after the relaxation process, there is an increase of the first peak value of RDF for both the single-tip and the multi-tip tool cutting, and the two RDF curves have nearly the same shape (as shown in Fig. 16b). This result is in good agreement with the CSP result as discussed above and indicates that local recrystallization takes place on the machined surface during the relaxation process.

Nevertheless, it is noted that the local recrystallization observed in the multi-tip tool cutting is more noticeable than the single-tip tool cutting. Although the thickness of the atomic defect layer before relaxation when using the multi-tip tool was much larger than that of using the single-tip tool, most of the defects were annealed and left almost an ideal FCC lattice structure after the relaxation process. As evident from Figs. 15b and 15d, the thickness of the residual atomic defect layers are 3.0 and 3.9 nm for the single-tip and the multi-tip tool cuttings, respectively.

4.3.8   Summary

This session was dedicated to provide a detailed understanding on the nanostructure generation processes when using a single-tip and a multi-tip diamond tool through
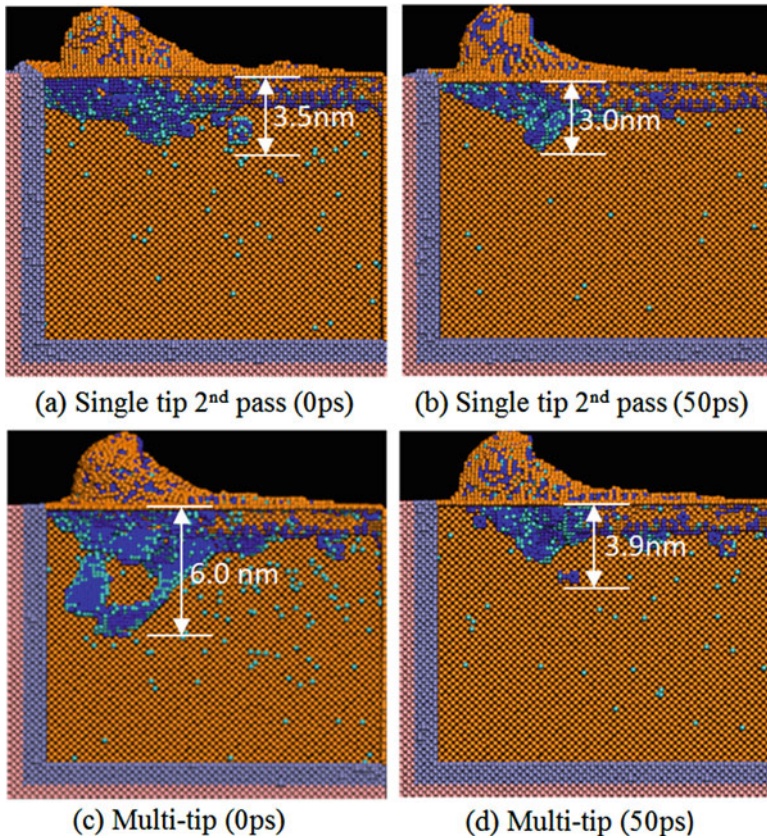
Fig. 15 The cross-sectional views of the defect zones after 0 and 50 ps relaxation process. Cyan and blue atoms represent particle dislocation and stacking fault, respectively (Tong et al. 2014b)

MD simulation studies. Compared with the single-tip cutting, the new features of multi-tip tool cutting such as the improved center line symmetry of machined nanostructures, the high cutting temperature, and the high normal cutting force per tip have been identified. The simulation results indicate that, in addition to the high machining efficiency, the effect of feed rate and the alignment issues on machining accuracy associated with the use of separate single-tip tool can be completely eliminated when using nanoscale multi-tip tools.

4.4   Influence of Processing Parameters

In diamond turning using nanoscale multi-tip diamond tools, as the tools and the machined structures are in a range of submicron or even dozens of nanometers, even tiny (nanometer-level) machining defects can degrade the form accuracy and the integrity of machined nanostructures. In-depth understanding of the machining process, especially knowing the nanomanufacturing capability under different cutting
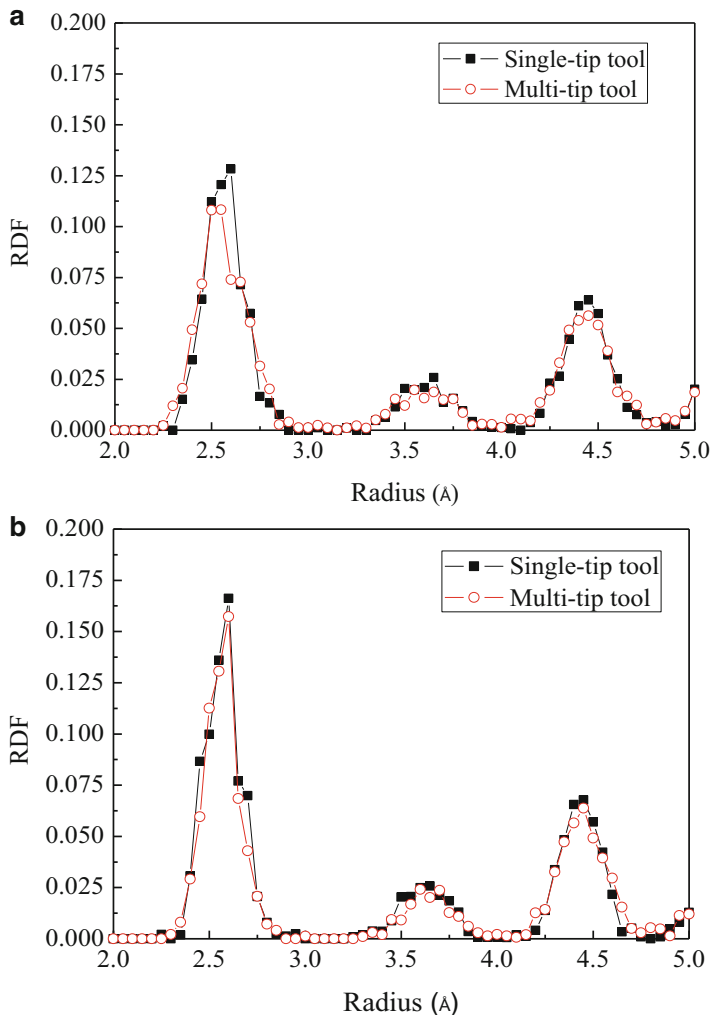
Fig. 16 RDF of machined nano-grooves. (**a**) Before the relaxation and (**b**) after 50 ps relaxation (Tong et al. 2014b)

conditions, is of great significance to the full exploration of the advancement of this technique. In this session, the focus will be on the influence of processing parameters on the accuracy and the integrity of machined nanostructures. A series of nanometric cutting trials (under 15 different cutting conditions) on copper substrates are carried out using the nanoscale multi-tip diamond tool fabricated with L/W_f of 1.54, which has been approved to possess the best shape transformability from the tool to the workpiece surface (Luo et al. 2014). In order to reveal the underlying mechanism for machining defects observed in experiments, MD simulations are also carried out to gain atomistic insight into the work material behavior during the nanometric cutting process.

Fig. 17 Experimental configuration and tooling setup (Tong et al. 2015a)
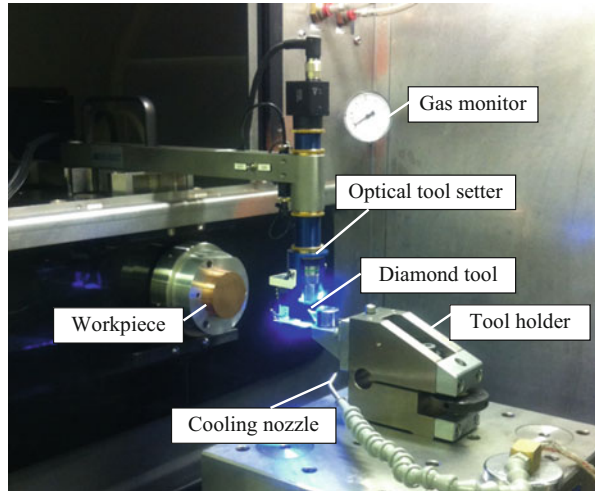
4.4.1 Experimental Setup

The nanometric face cutting trials using a nanoscale multi-tip diamond tool were carried out on a diamond turning machine (Precitech Nanoform 250). The configuration of the cutting trials is shown in Fig. 17. The cutting tools were mounted on a tool holder. An optical tool setter with a 20x long working distance objective lens was used to set the tools.

Nanometric machining was conducted on an oxygen-free copper (OFC) wafer. It had a diameter of 50 mm and the following properties: hardness 89HV50, density 8.94 g/cm^3, shear modules 44.0 GPa, Poisson's ratio 0.31, and annealing temperature 37–650 °C

Three-diamond cutting tools were used in the experiment. Before the multi-tip diamond tool cutting, a flat copper substrate surface was prepared by face diamond turning using two normal diamond tools. One conventional roughing tool was used for rough cutting of the copper surface. After the rough cutting, a controlled waviness diamond tool was used to generate the surface with mirror finish. The cutting fluid (CLAIRSOL 330 special kerosene) was applied in these steps. Then, the multi-tip diamond tool was used to generate nano-grooves on the flat copper surface. The multi-tip tool had a tip height of 589.8 nm, a tip width of 152.9 nm, and a tip base width of 458.5 nm with the tip distance being 706 nm. The geometrical features of the cutting tools are listed in Table 3.

Three spindle speeds tested were 12 rpm (low), 60 rpm (medium), and 120 rpm (high). For each spindle speed, the value of depth of cut was set at five different levels, from 100 nm to 500 nm with an increment of 100 nm. The parameters are list in Table 4.

The multi-tip diamond tool is fabricated by using a dual-beam FIB facility (FEI Quanta3D FEG). After the machining trials, the machined surface roughness and the nanostructure pattern were measured by using a white light interferometer (Form TalySurf CCI 3000) and a scanning electron microscope within the FEI Quanta3D FEG, respectively.

Table 3 Geometric features of the cutting tools used in the cutting trials (Tong et al. 2015a)

	Tool nose radius (mm)	Rake angle (°)	Clearance angle (°)	Cutting edge radius
Roughing tool	0.5	0	10	Standard
Controlled waviness tool	0.5	0	10	Standard
Nanoscale Multi-tip tool	–	0	10	40 nm

Table 4 Operational variables and their levels in face turning trials (Tong et al. 2015a)

Face cutting	No. of cut	Depth of cut (nm)	Spindle speed (rpm)	Radius of start point (mm)	Cutting speed (m/s)	Feed rate (μm/re)
Group A	1st	100	12	23.0	0.02890	9
	2nd	200	12	22.5	0.02827	9
	3rd	300	12	22.0	0.02765	9
	4th	400	12	21.5	0.02702	9
	5th	500	12	21.0	0.02639	9
Group B	6th	100	60	19.0	0.11938	9
	7th	200	60	18.5	0.11624	9
	8th	300	60	18.0	0.11310	9
	9th	400	60	17.5	0.10996	9
	10th	500	60	17.0	0.10681	9
Group C	11th	100	120	15.0	0.18850	9
	12th	200	120	14.5	0.18221	9
	13th	300	120	14.0	0.17593	9
	14th	400	120	13.5	0.16965	9
	15th	500	120	13.0	0.16336	9

4.4.2 MD Simulation Setup

The MD nanometric cutting model was developed as shown in Fig. 18 (Tong et al. 2015a). The geometrical parameters of the tool were built according to the shape of the multi-tip tool tips fabricated by FIB. The tool had a tip width W_a of $3a_1$ ($a_1 = 3.567$ Å), a tip base width W_f of $9a_1$, a tool rake angle α of $0°$, a tool clearance angle β of $10°$, a tip angle θ of $14°$, and a cutting edge radius r of $5a_1$. To save the computational time, a double-tip nanoscale diamond tool with the tool tip distance L of $14a_1$ was employed in present work to represent the nanoscale multi-tip diamond tool (as shown in Fig. 18a). The systems were controlled by NVE ensemble, and the thermostat atoms were kept at a constant temperature of 293 K through a velocity scaling method to perform the heat dissipation. The other computational parameters used in the MD simulations are summarized in Table 5 for reference.
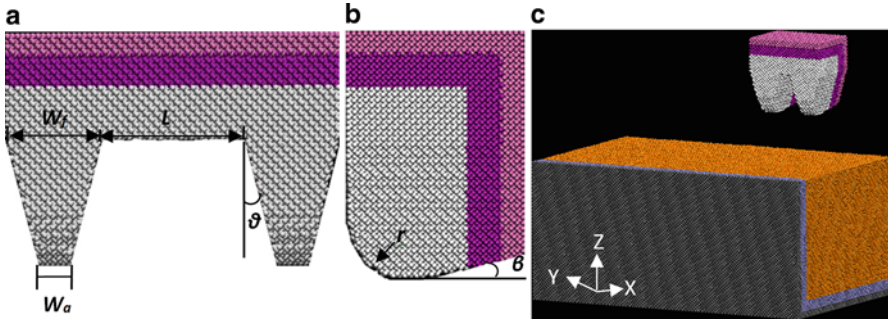
Fig. 18 Molecular dynamics simulation model: (**a**) Front view of the multi-tip tool model; (**b**) right-hand end elevation of the multi-tip tool model; and (**c**) nanometric cutting model (Tong et al. 2015a)

Table 5 Simulation parameters of MD nanometric cutting model (Tong et al. 2015a)

Workpiece materials	Copper
Workpiece dimensions	$50a_2 \times 80a_2 \times 40a_2$ ($a_2 = 3.615$ Å)
number of atoms	714,707
Time step	1 fs
Initial temperature	293 K
Depth of cut (cutting speed = 200 m/s)	2.0 nm, 2.5 nm, 3.0 nm, 3.5 nm, 4.0 nm
Cutting speed (depth of cut = 2.0 nm)	10 m/s, 50 m/s, 100 m/s, 160 m/s, 200 m/s, 250 m/s

4.4.3 Nanostructures Formed Under Different Cutting Conditions

As shown in Fig. 19a (Tong et al. 2015a), the surface roughness S_a of the copper substrate was 1.85 nm prepared by the face diamond turning. The surface was then machined by the nanoscale multi-tip diamond tool with a depth of cut of 100 nm (a cutting speed of 0.03 m/s, a feed rate of 9 μm/rev).

The SEM images of several machined grooves using different depths of cut are shown in Fig. 20 (Tong et al. 2015a). In general, the periodic nanostructures on the diamond tool tip were successfully replicated on the surface of the copper substrate when the depths of cut of 100 and 200 nm were used. As shown in Fig. 20a, the measured bottom widths of the nano-grooves generated under the depth of cut 100 nm ranged from 142.3 to 150.2 nm, which are slightly less than the tool tip width of 152.9 nm. The deviation is mainly due to the elastic recovery of the work material after the tool tip released from the surface. Moreover, the surface roughness S_a of the region between each cutting pass was found to be slightly increased to 2.50 nm (as shown in Fig. 19b), which is mainly caused by the material squeezed from the adjacent cutting passes.
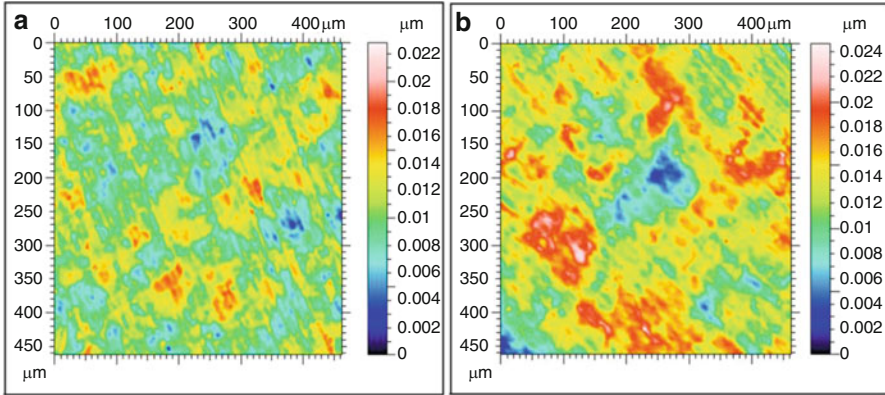
Parameters calculated on the surface before cutting (form removed, polynomial of order 2)

Parameters calculated on the surface after cutting (form removed, polynomial of order 2)

Amplitude Parameters:

Amplitude Parameters:

$S_a = 0.0018541$ μm; $S_q = 0.0023312$ μm

$S_a = 0.0025008$ μm; $S_q = 0.0031812$ μm

$S_z = 0.019278$ μm

$S_z = 0.019631$ μm

Fig. 19 The surface roughness of workpiece (**a**) before nanoscale multi-tip tool cutting and (**b**) after nanoscale multi-tip tool cutting (the lens was focused on the surface region between each cutting pass) (Tong et al. 2015a)

However, the form accuracy and integrity of the machined nano-grooves were found to be degraded with the increase of depth of cut. Lots of side burrs were observed when the depth of cut was equal or larger than 300 nm (Fig. 20c). Structure damage was found when a depth of cut of 400 nm was used (Fig. 20d). The results indicate that there exists an upper limit of depth of cut when machining nano-grooves using nanoscale multi-tip diamond tools.

The SEM images of nanostructures machined at different cutting speeds are shown in Fig. 21 (depth of cut = 100 nm). The results show that the form accuracy of the machined nano-grooves degrades with the increase of the cutting speed. No visible defect was found in the case of cutting speed being 0.03 and 0.12 m/s. However, side burrs were observed when the cutting speed increased to 0.18 m/s. A similar cutting speed effect was observed when a depth of cut of 200 nm was used (Fig. 22) (Tong et al. 2015a). However, under a large depth of cut of 300 nm (Fig. 23) (Tong et al. 2015a), the increase of high cutting speed finally resulted in a seriously structure damage.

Therefore, it can be concluded that the burr and the structure damage are the two major types of machining defects when improper processing parameters are used in the nanoscale multi-tip tool cutting. The atomistic insight into the work material behavior responsible for the formation of the machining defects will be discussed in the next section.
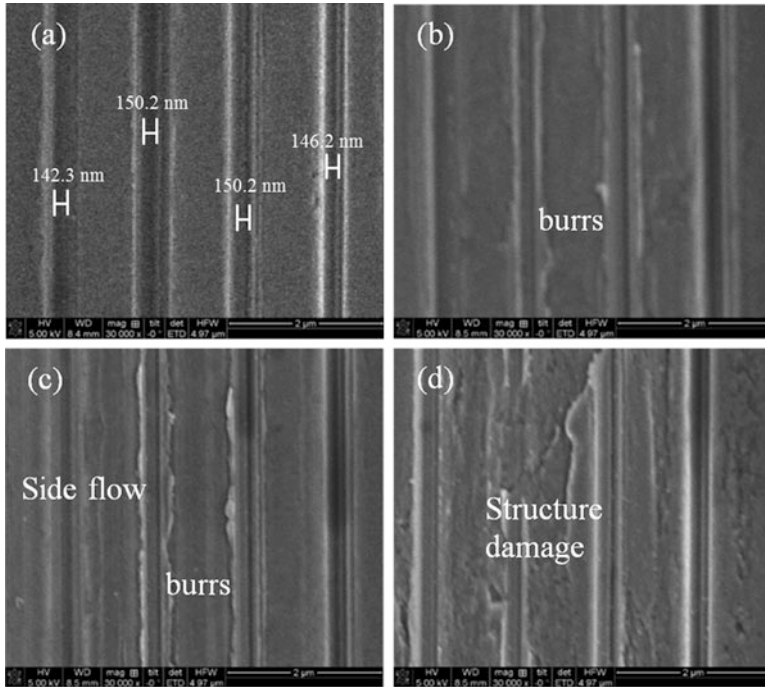
Fig. 20 SEM images of nano-grooves machined using different depths of cut (**a**) 100 nm, (**b**) 200 nm, (**c**) 300 nm (**d**) 400 nm (cutting speed = 0.03 m/s, feed rate = 9 μm/rev) (Tong et al. 2015a)

4.4.4 Effects of Depth of Cut

In order to reveal the underlying mechanism for machining defects, an MD nanometric cutting model was built to simulate the nanometric cutting process when using a nanoscale multi-tip diamond tool. For better comparison, a ratio of depth of cut to tip height (d/h) was employed when comparing the simulation results with the experimental results. The quality of the machined nanostructures was characterized by both the form accuracy of the machined nanostructures achieved in depth direction and the thickness of the deformed layers. The form error was calculated by the deviation of the depth of machined nano-groove to the design dimension.

The simulation results of machined nanostructures under different depths of cut are shown in Fig. 24 (Tong et al. 2015a). Two nano-grooves were successfully generated when a depth of cut of 2.0 nm (d/h = 0.46) was applied (Fig. 24a). However, as evident from Fig. 24b–e, the form accuracy is degraded with the further increase of the depth of cut. Apparent side burrs were observed on both edges of the machined nano-grooves. The form error of nano-grooves in the depth direction is 4.0% when a depth of cut of 2.5 nm was used. It increased to 20% when cutting under the depth of cut of 4.0 nm.
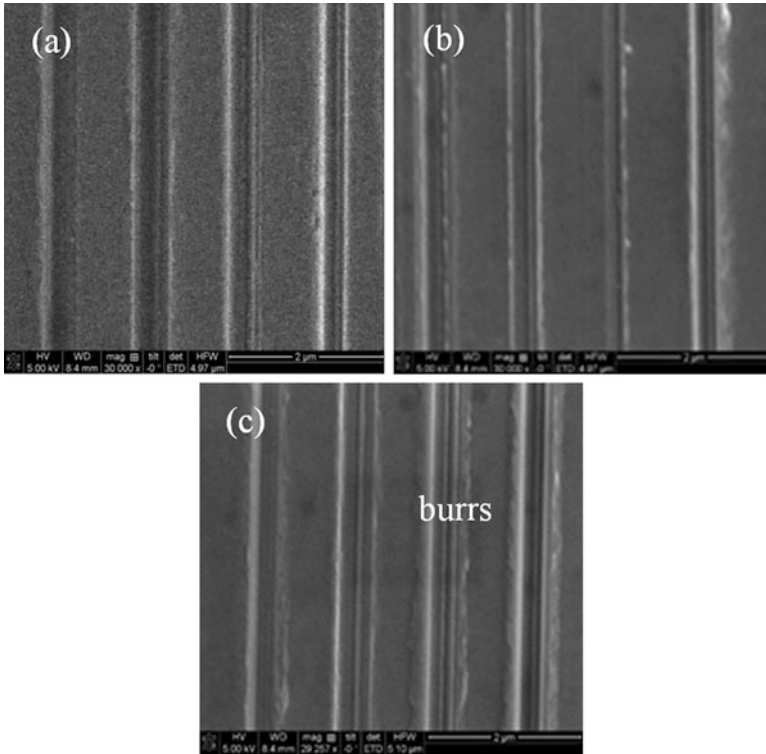
Fig. 21 SEM images of nano-grooves machined under different cutting speeds (**a**) 0.03 m/s, (**b**) 0.12 m/s, (**c**) 0.18 m/s (depth of cut = 100 nm, feed rate = 9 μm/rev) (Tong et al. 2015a)

Moreover, the wedge of cutting tool resulted in material pileups around tool tips. Visible material bulge between the machined nano-grooves was found when a depth of cut of 2.5 nm was used (Fig. 24b), mainly due to the overlap effect of the multi-tip tool cutting. However, with further increase of the depth of cut, the height of bulge reduced, and it disappeared when a depth of cut of 3.5 nm (d/h = 0.81) was applied (Fig. 24d). Apparently structure damage was found when a depth of cut of 4.0 nm (d/h = 0.93) was used (Fig. 24e).

The thicknesses of the deformed layer when using different depths of cut are shown in the middle column of Fig. 24. Significant dislocation pile-ups were observed beneath the tool tips. The larger the depth of cut, the larger the range of the deformed layer and the dislocations pile-ups were observed. The dislocation pile-ups would result in local strengthening of the work material in the normal direction. The resistance force makes work materials in front of each tip and between the tips flow up. This trend resulted in the built-up volume of each cutting tip merging into one big chip as shown in Fig. 24c–e. Due to the chip merging, the volume of chip and the height of the tool-chip separation point significantly increased. When the static friction force between the inner side of the tool tip and the workpiece is large enough, adhesion slip takes place and results in burrs and structure damage between the tool tips.
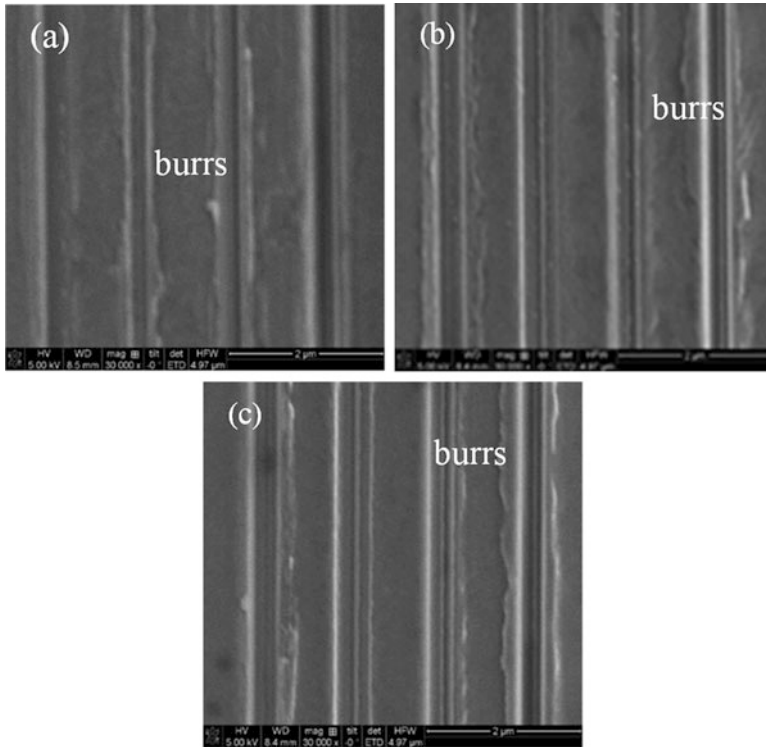
Fig. 22 SEM images of nano-grooves machined under different cutting speeds (**a**) 0.03 m/s, (**b**) 0.12 m/s, (**c**) 0.18 m/s (depth of cut = 200 nm, feed rate = 9 μm/rev) (Tong et al. 2015a)

In the experimental work (Fig. 20), the visible machining defects are observed when the depth of cut is equal and larger than 300 nm (d/h = 0.51). In the MD simulation, the critical value of d/h for the onset of visible form errors (larger than 13.3%) is 0.70. The ratio predicted by simulation is larger than the experimental result which is mainly due to the ideally perfect single crystal structure of copper material and the cutting tool assumed in the MD simulation model. In practice, a small depth of cut is usually a necessary condition of improving the machining precision (Neugebauer et al. 2012). The current experimental and simulation results indicate that this rule also works for the nanoscale multi-tip diamond tool cutting.

4.4.5 Effects of Cutting Speed

In order to obtain in-depth understanding of the effect of cutting speed observed in the experiments, simulations of a nanometric cutting process using a multi-tip tool were performed over a wide range of cutting speeds (10–250 m/s) using the same depth of cut of 2.0 nm.
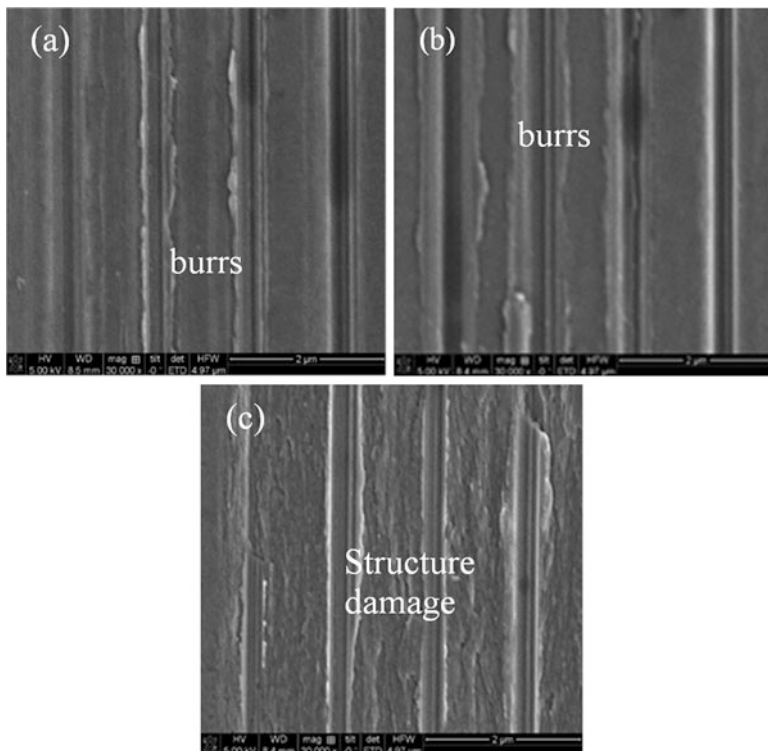
Fig. 23 SEM images of nano-grooves machined under different cutting speeds (**a**) 0.03 m/s, (**b**) 0.12 m/s, (**c**) 0.18 m/s (depth of cut = 300 nm, feed rate = 9 μm/rev) (Tong et al. 2015a)

As shown in Fig. 25 (Tong et al. 2015a), nano-grooves were indicated when the cutting speed was lower than 160 m/s. With the wedge of the cutting tool, each tip created a built-up volume around the tool tip. Although the tiny bulge of materials was observed when the cutting speed increased to 100 m/s, visible side burrs were found when the cutting speed was equal or higher than 200 m/s (Fig. 25e). Moreover, dislocation pile-ups were found when the cutting speed increased to 160 m/s (right column of Fig. 25). This phenomenon indicates that the overlap effect took place when a high cutting speed was used.

Figure 26 (Tong et al. 2015a) summarizes the distributions of local cutting temperatures under different cutting speeds. As expected, the range of the high-temperature region (>450 K) significantly increases with the cutting speed. The high cutting temperature would soften the work material at the cutting zone and extend the range of material plastic deformation zone, finally resulting in the overlap effect between the tool tips and the formation of the side burr. Although the range of the cutting speed used in simulations is still higher than the cutting speed used in experiment, the trend of the cutting speed effect obtained from simulations agreed with the experimental results qualitatively. The form accuracy of the machined nano-grooves degraded with the increase of cutting speed due to the formation of side burrs.
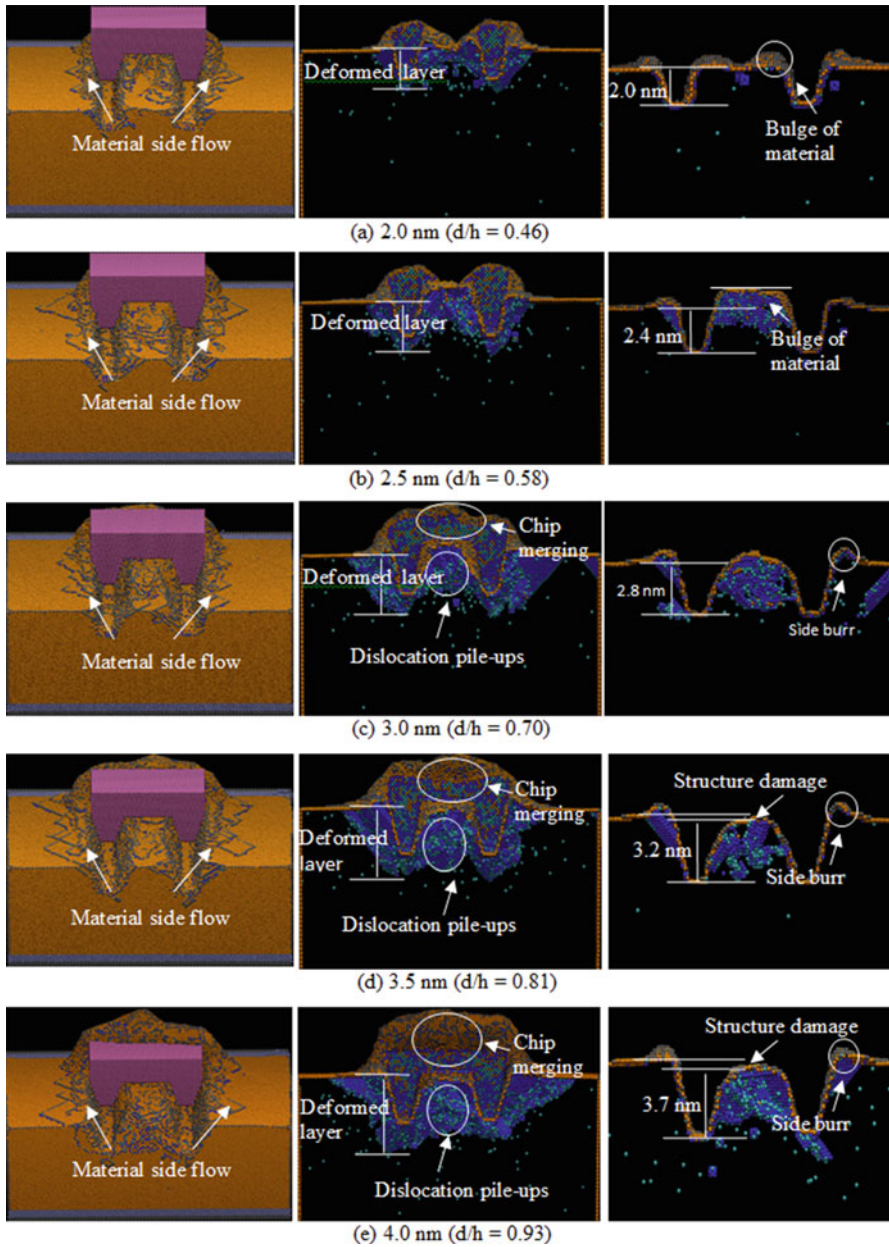
(a) 2.0 nm (d/h = 0.46)

(b) 2.5 nm (d/h = 0.58)

(c) 3.0 nm (d/h = 0.70)

(d) 3.5 nm (d/h = 0.81)

(e) 4.0 nm (d/h = 0.93)

Fig. 24 MD simulation results of machined nanostructures (left), the cross-sectional views of deformed layers (middle), and the cross-sectional views of machined nano-grooves (right) using different depths of cut: (**a**) 2.0 nm, (**b**) 2.5 nm, (**c**) 3.0 nm, (**d**) 3.5 nm, (**e**) 4.0 nm (Tong et al. 2015a)
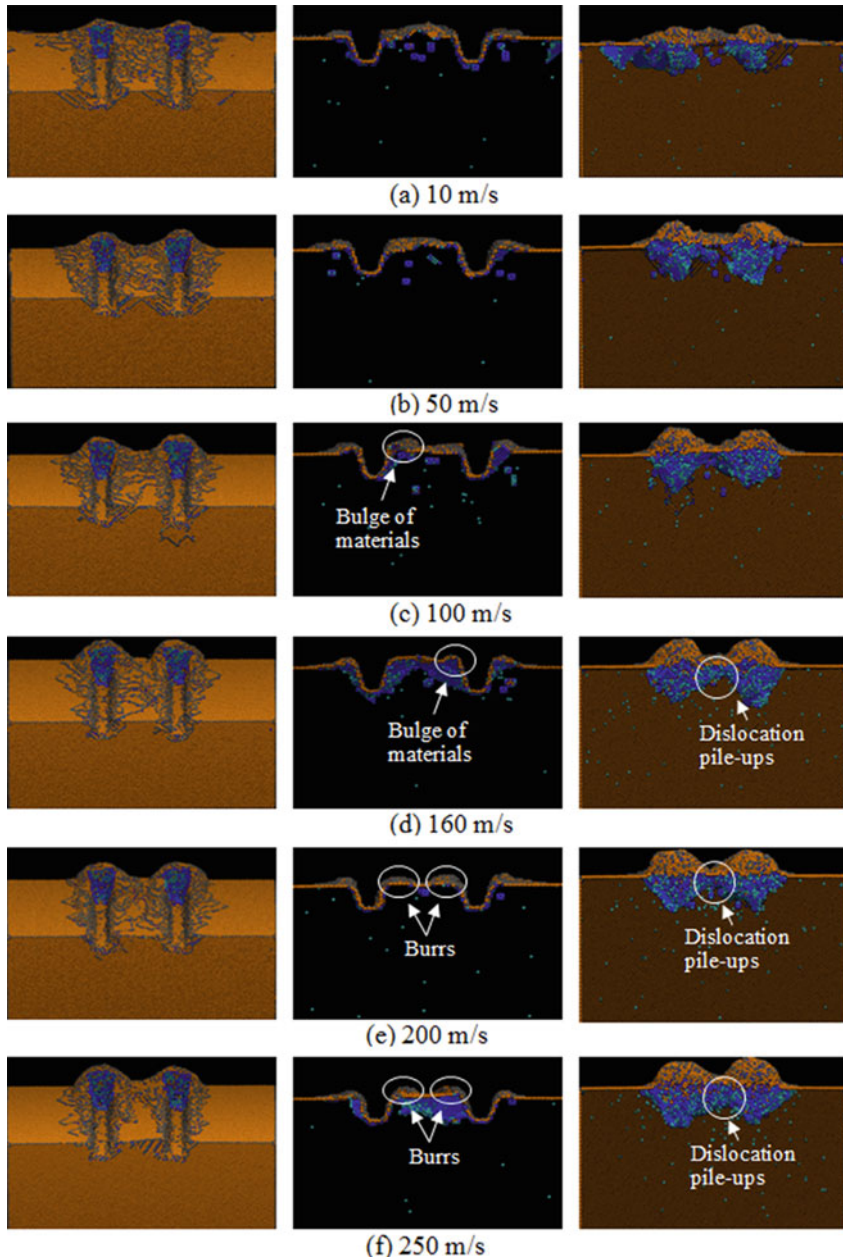
Fig. 25 The MD simulation results of nanostructures formed using the cutting speed of (**a**) 10 m/s, (**b**) 50 m/s, (**c**) 100 m/s, (**d**) 160 m/s, (**e**) 200 m/s, and (**f**) 250 m/s. The left column shows the surface of machined nanostructures; the middle column shows the cross-sectional view of formed nanostructures; the right column shows the inside view of the dislocation distribution under the cutting tool tips (Tong et al. 2015a)
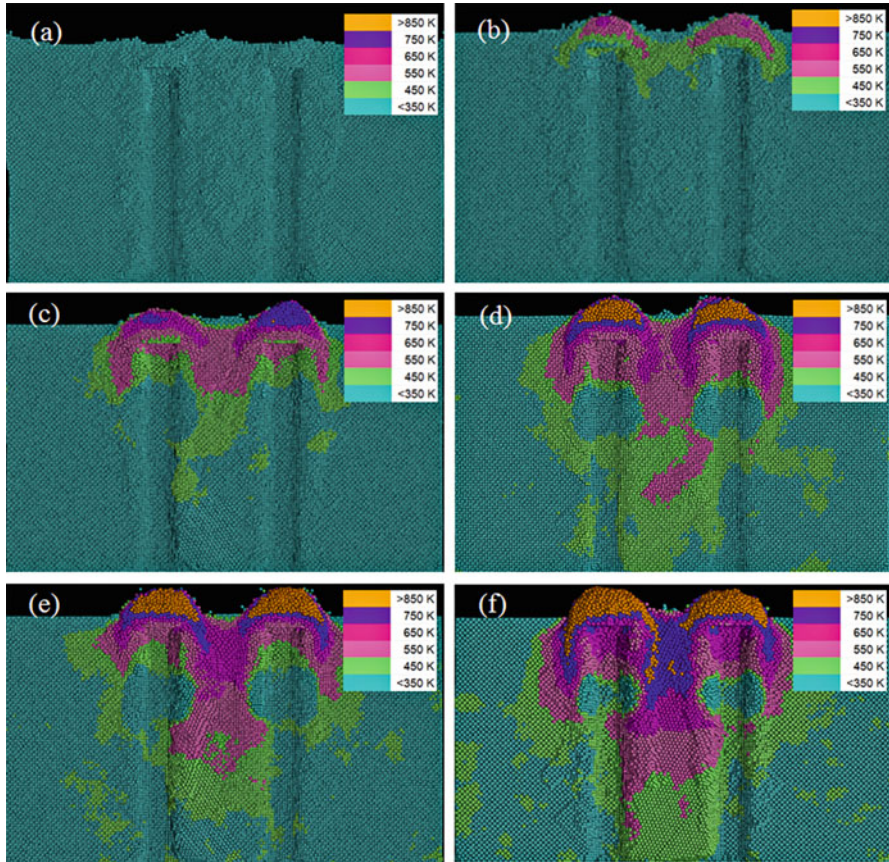
Fig. 26 Temperature distribution under different cutting speeds (**a**) 10 m/s, (**b**) 50 m/s, (**c**) 100 m/s, (**d**) 160 m/s, (**e**) 200 m/s, (**f**) 250 m/s (Tong et al. 2015a)

Nevertheless, it is noted that the form errors of the machined nanostructures in depth direction are all less than 5% for the cutting speed applied. Visible side burrs were observed only when the dislocation pile-ups took place. Thus it is predicted that, in nanoscale multi-tip tool cutting, there is a critical cutting speed below which the overlap effect can be ignored in machining nanostructures under a certain acceptable accuracy. More nanometric cutting experiments need to be carried out in the future for a fully quantitative validation.

4.4.6 Summary

In this session both nanometric cutting experiments and MD simulations have been carried out to study the processing capability of diamond turning using a nanoscale multi-tip diamond tool. It found that the operational parameters significantly affect

the quality of the machined nanostructures. The high-precision nanostructures were successfully produced by diamond face cutting under a depth of cut of 100 nm and a cutting speed of 0.03 m/s. Under the studied cutting conditions, the burr and structure damage are the two major types of machining defects. The formation of machining defects has been emulated by MD simulations. The investigation showed that with the increase of the depth of cut and the cutting speed, the increasing overlap effect between the tool tips is responsible for the formation of side burr and structural damage.

4.5   Tool Wear

As in other ultra-precision diamond turning processes, tool wear is also a big concern when using nanoscale multi-tip diamond tool for nano-grooving. The SEM images of the nanoscale multi-tip diamond tool before and after the cutting trials are shown in Fig. 27 (Tong et al. 2015a). Unlike the conventional single-tip diamond tool cutting where the initial tool wear was mostly found at the clearance face near the tool cutting edges, the tool wear in the multi-tip tool cutting was found on both the

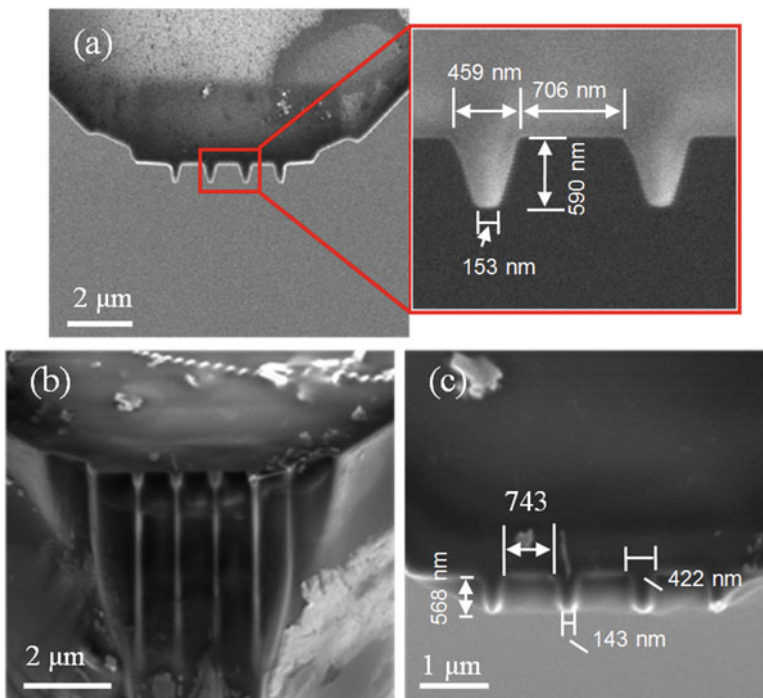**Fig. 27** SEM images of the nanoscale multi-tip diamond tool. (**a**) SEM image of the tool before cutting, (**b**) SEM image of the tool cutting edges after cutting, and (**c**) a close-up view of the shape of tool tips after cutting (Tong et al. 2015a)

clearance face and the sides of the tool tips after a cutting distance of 2.5 km. No visible wear marks were observed at the rake face of the tool tips. The measured tip distance enlarged from 706 to 743 nm because of the wear on the sides of the tool tips. The main reason of tool wear is that for multi-tip tool cutting, the nanostructures are formed synchronously within a single cutting pass. The sides of the tool tips are involved in the formation of nanostructures. The compressive stress produced at the sides of the tool tips results in the friction between the tool tip and workpiece and thus results in the initiation of tool wear in this region.

Moreover, the tool wear is closely related to the local cutting temperature. Many research works have emphasized the significance of thermal effects on tool wear and suggested that an important way to control the tool wear is to reduce the cutting temperature in the cutting zone (Tong et al. 2014b; Ikawa et al. 1991b; Cheng et al. 2003). Figure 28a–c (Tong et al. 2015a) suggests the temperature distributions of tool tips for different depths of cut obtained by MD simulations. It is found that the temperature was uniformly distributed at the tool tip when a small depth of cut of 2.0 nm was used. However, when cutting under a depth of cut of 3.0 nm, a high local temperature (>620 K) was generated both at the cutting edges and the side edges of the tool tips. Similar results were observed when the depth of cut increased to 4.0 nm. This high local temperature would soften the C–C bonds and accelerate the tool wear process in these regions.

In addition, it has been shown that a high cutting speed will apparently increase the cutting temperature at the cutting zone. It is anticipated that the tool wear rate will increase with the cutting speed as well.

Usually, the progressive thermochemical wear of a diamond tool is mainly attributed to the oxidation, graphitization, diffusion, and carbide formation during the long-term cutting process. For FIB-shaped diamond tools, the ion irradiation-induced doping and defects will also degrade the property of cutting tools. A previous study by Tong et al. on ion-induced damaged layer during tool fabrication process has shown that the energetic ion collision can result in an amorphous carbon layer around the tool tips (Tong et al. 2015b). This damaged layer would increase the adhesion between tool and work materials (Kawasegi et al. 2014a). As schematically shown in Fig. 29, during the nanometric cutting process, the FIB-induced damaged layer was expected to worn away firstly because of its non-diamond phase. Most recently, a similar phenomenon has been reported in micro-machining of NiP using a FIB-irradiated single-tip diamond tool (Kawasegi et al. 2014a, b). The present study, for the first time, provides significant information about the initial tool wear in the nanometric cutting of copper using a nanoscale multi-tip diamond tool. More research work needs to be carried out in the future to obtain a sufficient data for building a rigorous tool-life management and prediction program.

To sum up, due to the limitation of current computational power, performing MD simulation on nanometric cutting with the same physical size and small cutting speed used in experiments remains a big challenge, especially for the large-scale MD model built in present work. However, this does not affect our analysis of the general nature of machining. Although it is not possible to have quantitative comparison to
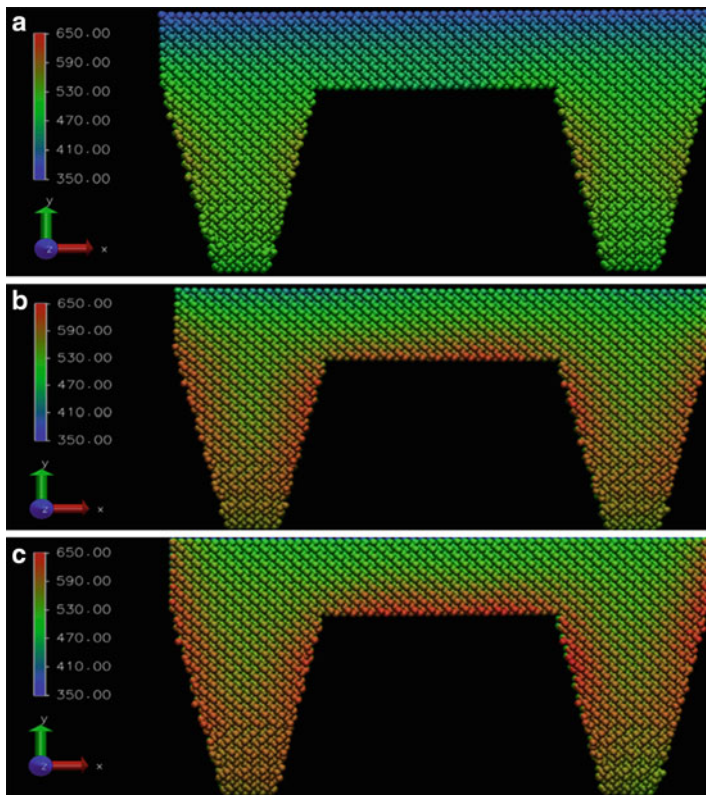
Fig. 28 MD simulation results of the temperature distributions on the nanoscale multi-tip diamond tools for different depths of cut. (**a**) 2 nm, (**b**) 3.0 nm, and (**c**) 4.0 nm (Tong et al. 2015a)
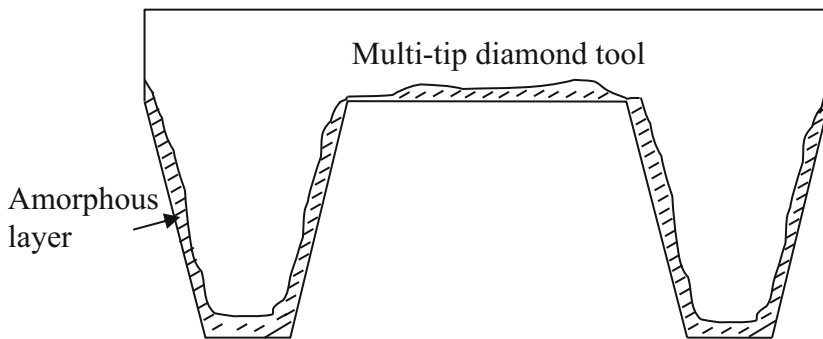

Fig. 29 Schematic illustration of the early tool wear region of a multi-tip diamond tool resulting from FIB-induced damage (Tong et al. 2015a)

the experimental measurement, the MD nanometric cutting model allows the atomistic insight into the work material behavior and reveals the underlying mechanisms for the machining defects as well as the tool wear during nanometric cutting process. The research findings obtained from MD simulations can help interpret the experimental data. The present analysis will be valuable to any nanomanufacturing practice where a nanoscale multi-tip diamond tool is used. Therefore, if the full advantages of nanometric cutting using multi-tip diamond tool predicated by the MD simulations are to be realized, selection of parameters used in tool fabrication, optimal design of tool geometry, and optimization of processing parameters used in nanometric cutting practice are critical to provide high-performance and efficient machining when using nanoscale multi-tip diamond tools. The FIB-induced damaged layer, the cutting speed, and the depth of cut have significant effects on the tool wear. Based on the obtained results, it is reasonable to anticipate that, in nanoscale multi-tip tool cutting, high-precision nanostructures can be achieved under an optimal cutting condition where the overlap effect can be ignored in the nanostructure generation process.

4.6   Concluding Remarks

Currently, it is still quite difficult to compare MD simulations with experimental results in the same spatial and time scale. From the MD simulation side, the difficulties lie in developing a super high-performance computing system for solving a highly inhomogeneous multibody problem having the same spatial and time scales as experiments, as well as an effective visualization technique for analyzing the large-scale MD simulation results. The difficulties from the experimental side have been the limitation of using FIB to fabricate multi-tip diamond tool with tool tips in several nanometers, and the time resolution that is needed for a detection equipment to capture the transient process of defect formation which evolve on time scales of some nanoseconds.

However, current MD simulation results show that the mechanisms of nanostructure formation by using single-tip tools and multi-tip tools are different. Compared with the single-tip tool cutting, a higher cutting temperature and a higher average normal cutting force per tip were found in the multi-tip tool cutting. Since the nanostructures are synchronously formed by a single cutting pass, the effects of feed rate and the alignment issues associated with the use of single-tip tools can be completely eliminated when using nanoscale multi-tip tools. This unique feature makes the multi-tip tool cutting more practicable and applicable than the single-tip cutting for scale-up fabrication of periodic nanostructures. Owing to the unprecedented merits of high throughput, one-step, and highly flexible precision capabilities, this technique has led to the hope for breaking the technical bottleneck for the scale-up manufacturing nanostructures.

The operational parameters significantly affect the quality of the machined nanostructures. The high-precision nanostructures were successfully produced by diamond face cutting under a depth of cut of 100 nm and a cutting speed of 0.03 m/s.

An optimization of the cutting conditions, by which the overlap effect can be ignored in the nanostructure generation process, is recommended in the future work to obtain high-precision nanostructures when using nanoscale multi-tip diamond tools.

The tool wear is initially found at both the clearance cutting edge and the side edges of tool tips after a cutting distance of 2.5 km. The FIB-induced damaged layer (Tong et al. 2015b) and the friction produced at each side of the tool tip are responsible for the tool wear.

To systematically establish this nano-grooving approach, the following work is thought to be performed in the near future:

1. Developing an Effective Post-processing Method for Tool Fabrication
   The study carried out by Tong and co-workers (Tong et al. 2015b) on FIB-induced damage in diamond has demonstrated that the energetic ion collision can result in a damaged zone (a mixture phase of sp^2 and sp^3 hybridization and the implanted gallium), which is much larger than the defined ion irradiated area, even under the low-beam energy of 8 kV. Most recently, it has been reported that the doping of gallium ions at tool rake face would result in a rapid diamond tool wear due to the increase of the adhesion of work materials to the tool surface (Kawasegi et al. 2014b). Thus, the ion irradiation-induced doping and defects will unavoidably degrade the cutting performance of the micro- and nanoscale diamond tools fabricated by FIB. An effective post-processing method which is able to remove/minimize the damaged layers after FIB machining is in high demand. The minimization of the FIB-induced damaged layer will become more important when the dimensions of a multi-tip diamond tool are approaching their ultimate values.

2. Optimization of the Design of Multi-tip Diamond Tools
   It is widely known in conventional cutting that the tool geometrical parameters such as the rake angle, clearance angle, and the cutting edge radius can influence the material removal process. The research work done by Tong et al. indicates that, the unique tool geometrical parameters of a multi-tip tool including the tool-tip distance, tip angle, and tip configuration can play an important role in achieving high the accuracy of the machined nanostructures (Luo et al. 2014). It seems to be a complex interplay of all these variables in order to obtain a deterministic fabrication of high-quality nanostructures. Therefore, an optimization of the tool design by considering all these parameters can further improve the shape transferability of multi-tip diamond tools in an SPDT operation.

3. Setting up a Processing Database of the Multi-tip Tool Cutting
   The processing parameters such as depth of cut and cutting speed significantly affect the attainable integrity of machined nanostructures as well as the tool life. Due to the limitations of time and the high research cost of using relevant equipment, the experimental results obtained in the present study were not sufficient to set up a processing database for the nanometric cutting of copper using nanoscale multi-tip diamond tools. Currently, the processing parameters such as the maximum feed rate, depth of cut, and cutting speed for a specialized workpiece material have not yet been established. For the commercialization of

this technique in industry, more research work needs to be carried out in the future to obtain sufficient database for building a rigorous tool-life management and predication program and eventually an expert system for intelligently selecting optimal processing parameters for the cost-effective scale-up manufacturing of nanostructures.

References

Akimov YA, Koh W (2010) Resonant and nonresonant plasmonic nanoparticle enhancement for thin-film silicon solar cells. Nanotechnology 21:235201

Atwater HA, Polman A (2010) Plasmonics for improved photovoltaic devices. Nat Mater 9:205–213

Balamane H, Halicioglu T, Tiller W (1992) Comparative study of silicon empirical interatomic potentials. Phys Rev B 46:2250

Bartolo P, Kruth JP, Silva J, Levy G, Malshe A, Rajurkar K et al (2012) Biomedical production of implants by additive electro-chemical and physical processes. CIRP Ann Manuf Technol 61:635–655

Berman D, Krim J (2013) Surface science, MEMS and NEMS: Progress and opportunities for surface science research performed on, or by, microdevices. Prog Surf Sci 88:171–211

Cheng K, Luo X, Ward R, Holt R (2003) Modeling and simulation of the tool wear in nanometric cutting. Wear 255:1427–1432

Clark AW, Cooper JM (2011) Nanogap ring antennae as plasmonically coupled SERRS substrates. Small 7:119–125

Davies MA, Evans CJ, Vohra RR, Bergener, BC, Patterson SR (2003) Application of precision diamond machining to the manufacture of microphotonics components. In: Proceedings of SPIE, 2003

Daw MS, Foiles SM, Baskes MI (1993) The embedded-atom method: a review of theory and applications. Mater Sci Rep 9:251–310

Ding X, Lim G, Cheng C, Butler DL, Shaw K, Liu K et al (2008) Fabrication of a micro-size diamond tool using a focused ion beam. J Micromech Microeng 18:075017

Ding X, Jarfors A, Lim G, Shaw K, Liu K, Tang L (2012) A study of the cutting performance of poly-crystalline oxygen free copper with single crystalline diamond micro-tools. Precis Eng 36:141–152

Fang TH, Weng CI, Chang JG (2002) Molecular dynamics simulation of nano-lithography process using atomic force microscopy. Surf Sci 501:138–147

Friedrich CR, Vasile MJ (1996) Development of the micromilling process for high-aspect-ratio microstructures. J Microelectromech Syst 5:33–38

Friedrich C, Coane P, Vasile MJ (1997) Micromilling development and applications for micro-fabrication. Microelectron Eng 35:367–372

Holmberg S, Perebikovsky A, Kulinsky L, Madou M (2014) 3-D Micro and nano technologies for improvements in electrochemical power devices. Micromachines 5:171–203

Ikawa N, Shimada S, Tanaka H, Ohmori G (1991a) An atomistic analysis of nanometric chip removal as affected by tool-work interaction in diamond turning. CIRP Ann Manuf Technol 40:551–554

Ikawa N, Donaldson R, Komanduri R, König W, McKeown P, Moriwaki T et al (1991b) Ultra-precision metal cutting – the past, the present and the future. CIRP Ann Manuf Technol 40:587–594

Kaur IP, Singh H (2014) Nanostructured drug delivery for better management of tuberculosis. J Control Release 184:36–50

Kawasegi N, Niwata T, Morita N, Nishimura K, Sasaoka H (2014a) Improving machining performance of single-crystal diamond tools irradiated by a focused ion beam. Precis Eng 38:174–182

Kawasegi N, Ozaki K, Morita N, Nishimura K, Sasaoka H (2014b) Single-crystal diamond tools formed using a focused ion beam: tool life enhancement via heat treatment. Diam Relat Mater 49:14–18

Kelchner CL, Plimpton S, Hamilton J (1998) Dislocation nucleation and defect structure during surface indentation. Phys Rev B 58:11085

Komanduri R, Chandrasekaran N, Raff L (2000) Molecular dynamics simulation of atomic-scale friction. Phys Rev B 61:14007

Komanduri R, Chandrasekaran N, Raff L (2001) Molecular dynamics simulation of the nanometric cutting of silicon. Philos Mag B 81:1989–2019

Lin Z, Huang J (2008) A study of the estimation method of the cutting force for a conical tool under nanoscale depth of cut by molecular dynamics. Nanotechnology 19:115701

Liu Z, Steele JM, Srituravanich W, Pikus Y, Sun C, Zhang X (2005) Focusing surface plasmons with a plasmonic lens. Nano Lett 5:1726–1729

Luan B, Robbins MO (2005) The breakdown of continuum models for mechanical contacts. Nature 435:929–932

Luo X, Tong Z, Liang Y (2014) Investigation of the shape transferability of nanoscale multi-tip diamond tools in the diamond turning of nanostructures. Appl Surf Sci 321:495–502

Mokkapati S, Beck F, Polman A, Catchpole K (2009) Designing periodic arrays of metal nanoparticles for light-trapping applications in solar cells. Appl Phys Lett 95:053115

Neugebauer R, Drossel W, Wertheim R, Hochmuth C, Dix M (2012) Resource and energy efficiency in machining using high-performance and hybrid processes. Procedia CIRP 1:3–16

Norouzifard V, Hamedi M (2014) Experimental determination of the tool–chip thermal contact conductance in machining process. Int J Mach Tools Manuf 84:45–57

Pei Q, Lu C, Lee H, Zhang Y (2009) Study of materials deformation in nanometric cutting by large-scale molecular dynamics simulations. Nanoscale Res Lett 4:444–451

Pelaz L, Marqués LA, Barbolla J (2004) Ion-beam-induced amorphization and recrystallization in silicon. J Appl Phys 96:5947–5976

Picard YN, Adams D, Vasile M, Ritchey M (2003) Focused ion beam-shaped microtools for ultra-precision machining of cylindrical components. Precis Eng 27:59–69

Smith R, Kenny SD, Ramasawmy D (2004) Molecular dynamics simulations of sputtering. Philos Trans R Soc London, Ser A 362:157–176

Sun J, Luo X (2014) Chapter 7: deterministic fabrication of micro-and nanostructures by focused ion beam. In: Wang ZM (ed) Lecture notes in nanoscale science and technology. Springer, New York, pp 161–204

Sun J, Luo X, Chang W, Ritchie J, Chien J, Lee A (2012) Fabrication of periodic nanostructures by single-point diamond turning with focused ion beam built tool tips. J Micromech Microeng 22:115014

Tersoff J (1989) Modeling solid-state chemistry: interatomic potentials for multicomponent systems. Phys Rev B 39:5566

Tong Z, Liang Y, Jiang X, Luo X (2014a) An atomistic investigation on the mechanism of machining nanostructures when using single tip and multi-tip diamond tools. Appl Surf Sci 290:458–465

Tong Z, Liang Y, Yang X, Luo X (2014b) Investigation on the thermal effects during nanometric cutting process while using nanoscale diamond tools. Int J Adv Manuf Technol 74:1709–1718

Tong Z, Luo X, Sun J (2015a) Investigation of a scale-up manufacturing approach for nanostructures by using a nanoscale multi-tip diamond tool. Int J Adv Manuf Technol 80(1-4): 699–710

Tong Z, Xu Z, Wu W, Luo X (2015b) Molecular dynamics simulation of low-energy FIB radiation induced damage in diamond. Nucl Inst Methods Phys Res B 358:38–44

Vasile MJ, Friedrich CR, Kikkeri B, McElhannon R (1996) Micrometer-scale machining: tool fabrication and initial results. Precis Eng 19:180–186

Vasile MJ, Nassar R, Xie J, Guo H (1999) Microfabrication techniques using focused ion beams and emergent applications. Micron 30:235–244

Xu Z, Fang F, Zhang S, Zhang X, Hu X, Fu Y et al (2010) Fabrication of micro DOE using micro
    tools shaped with focused ion beam. Opt Express 18:8025–8032
Yan Y, Sun T, Dong S, Liang Y (2007) Study on effects of the feed on AFM-based nano-scratching
    process using MD simulation. Comput Mater Sci 40:1–5
Ye Y, Biswas R, Morris J, Bastawros A, Chandra A (2003) Molecular dynamics simulation of
    nanoscale machining of copper. Nanotechnology 14:390
Zhang S, Fang F, Xu Z, Hu X (2009) Controlled morphology of microtools shaped using focused
    ion beam milling technique. J Vac Sci Technol B 27:1304–1309
Zhu PZ, Hu YZ, Ma TB, Wang H (2010) Study of AFM-based nanometric cutting process using
    molecular dynamics. Appl Surf Sci 256:7160–7165
Zong W, Li Z, Sun T, Cheng K, Li D, Dong S (2010) The basic issues in design and fabrication of
    diamond-cutting tools for ultra-precision and nanometric machining. Int J Mach Tools Manuf
    50:411–419